ABSTRACT

PHYSICAL CONTROLS ON WATER FLOW AND SOLUTE TRANSPORT IN COASTAL AQUIFERS

by
Xiaolong Geng

Groundwater flow and associated subsurface solute fates have a significant impact on the structure and productivity of near-shore coastal ecosystems. For proper assessment and management of these coastal groundwater resources, it is quite essential to investigate the key factors (tides, waves, evaporation, and freshwater recharge etc.) affecting coastal groundwater systems. The main objective of this study is to examine and quantify two important physical control factors, oceanic waves and evaporation, on the groundwater flow and solute transport in near-shore aquifers. For the investigation of wave effects, a Computational Fluid Dynamics (CFD) modeling tool, Fluent, is used to simulate wave-induced sea level oscillations. A flow-averaged approach is developed to generalize wave motions acting onto the beach for the sake of the feasibility of numerical computation. A two-dimensional numerical model MARUN is used to simulate variably saturated, variable density groundwater flow and subsurface solute transport in coastal aquifers. To investigate evaporation effects, a classic bulk aerodynamic formulation is adopted as a module to the model MARUN for simulating groundwater flow and subsurface solute transport in bare saline soils subjected to transient evaporation. The simulation results reveal that these two factors significantly impact beach hydrodynamics. Wave forcing induces pore water circulations in the swash zone of the near-shore aquifers; wave forcing also modifies the pathways of solute transport in the beach prior to discharge into the ocean, and subsequently impacts plume's residence time, migration speed, discharge

location, and discharge rate. The evaporation decreases the moisture at shallow layer of the beach and subsequently impacts the subsurface salinity distribution.

PHYSICAL CONTROLS ON WATER FLOW AND SOLUTE TRANSPORT IN COASTAL AQUIFERS

by
Xiaolong Geng

A Dissertation
Submitted to the Faculty of
New Jersey Institute of Technology
in Partial Fulfillment of the Requirements for the Degree of
Doctor of Philosophy in Environmental Engineering

Department of Civil and Environmental Engineering

May 2014

.

APPROVAL PAGE

PHYSICAL CONTROLS ON WATER FLOW AND SOLUTE TRANSPORT IN COASTAL AQUIFERS

Xiaolong Geng

Dr. Michel C. Boufadel, Dissertation Advisor — Date
Professor of Civil and Environmental Engineering, NJIT

Dr. Nancy L. Jackson, Committee Member — Date
Professor of Chemistry and Environmental Science, NJIT

Dr. Lisa B. Axe, Committee Member — Date
Professor of Civil and Environmental Engineering, NJIT

Dr. Robert Dresnack, Committee Member — Date
Professor of Civil and Environmental Engineering, NJIT

Dr. Wen Zhang, Committee Member — Date
Assistant Professor of Civil and Environmental Engineering, NJIT

BIOGRAPHICAL SKETCH

Author: Xiaolong Geng

Degree: Doctor of Philosophy

Date: May 2014

Undergraduate and Graduate Education:

- Doctor of Philosophy in Environmental Engineering,
  New Jersey Institute of Technology, Newark, NJ, 2014

- Master of Applied Mathematics,
  Liaoning Normal University, Dalian, P. R. China, 2008

- Bachelor of Mathematics,
  Liaoning Normal University, Dalian, P. R. China, 2005

Major: Environmental Engineering

Journal Publications:

Xiaolong Geng, and Michel C. Boufadel. Numerical modeling of water flow and salt transport in bare saline soil subjected to transient evaporation (In preparation).

Xiaolong Geng, Michel C. Boufadel, Nancy L. Jackson, Richard S. Miller, and Hailong Li. Numerical study of solute transport in shallow beach aquifers subjected to waves and tides (In preparation).

Xiaolong Geng, Firas Saleh, Ali Abdollahi-Nasab, and Michel C. Boufadel. High pressure injection of chemicals in an oil-contaminated beach and its implication on bioremediation: Exxon Valdez oil spill case study, *Environmental Monitoring and Assessment* (submitted).

Michel C. Boufadel, A. Abdollahi-Nasab, **Xiaolong Geng**, and Jerry Galt. Time history of the Deepwater Horizon oil deposition on the shorelines of the Gulf of Mexico, *Environmental Science & Technology* (submitted).

Yves Robert Personna, **Xiaolong Geng**, Firas Saleh, and Michel C. Boufadel. Monitoring changes in salinity and metal concentrations in New Jersey coastal ecosystems oost-hurricane sandy, *Environmental Earth Sciences* (submitted).

Firas Saleh, **Xiaolong Geng**, and Michel C. Boufadel, Deep subsurface chemicals injection for the development of a feasible bioremediation technique: Exxon Valdez oil spill case study, *Hydrology of Coastal Research* (submitted).

Xiaolong Geng, Michel C. Boufadel, Yuqiang Xia, Hailong Li, and Lin Zhao. Numerical study of wave effects on groundwater flow and solute transport in a laboratory beach, *Journal of Contaminant Hydrology* (in Revision).

Xiaolong Geng, Michel C. Boufadel, Yves Personna, Ken Lee, David Tsao, and Erik D. Demicco, 2014. BioB: A mathematical modeling for the biodegradation of low solubility hydrocarbons, *Marine Pollution Bulletin* (in Press).

Xiaolong Geng, Nicholas C. Davatzes, Daniel J. Soeder, Jagadish Torlapati, Rebecca S. Rodriguez, and Michel C. Boufadel, 2013. Migration of high-pressure air during gas drilling in the Appalachian Basin, *Journal of Environmental Engineering*, http://dx.doi.org/10.1061/(ASCE)EE.1943-7870.0000769.

Xiaolong Geng, Michel C. Boufadel, Brian Wrenn, 2012. Mathematical modeling of the biodegradation of residual hydrocarbon in a variably-saturated sand column. *Biodegradation*, 24(2): 153-163.

Xiaolong Geng, Hailong Li, Michel C. Boufadel, Liu Shuang, 2009. Tide-induced head fluctuations in a coastal aquifer: effects of the elastic storage and leakage of the submarine outlet-capping level. *Hydrogeology Journal*, 17(5): 1289-1296.

Hailong Li, Yuqiang Xia, **Xiaolong Geng**, 2013. A comparison study of hydrology and hydrochemistry along two transects in mangrove tidal marsh at Dongzhaigang national nature reserve, Hainan, China. *Groundwater in Coastal Zones of Asia-Pacific*, 7: 11-25.

Pingping Sun, Hailong Li, Michel C. Boufadel, **Xiaolong Geng**, and Shi Chen, 2008. An analytical solution and case study of groundwater head response to dual tide in an island leaky confined aquifer. *Water Resource Research* 44(12): DOI: 10. 1029/2008WR006893.

Conferences Proceedings:

Xiaolong Geng, and Michel C. Boufadel, 2014. Modeling biodegradation of subsurface oil in a sandy beach polluted with the Deepwater Horizon oil spill, *International Oil Spill Conference*, Savannah, Georgia, USA (accepted).

Xiaolong Geng, and Michel C. Boufadel, 2013. A numerical model for simulating transient evaporation from bare saline soil, *The Third Asia-Pacific Coastal Aquifer Management Meeting*, Beijing, China.

Xiaolong Geng, Michel C. Boufadel, Nicholas C. Davatzes, Daniel J. Soeder, and Jagadish Torlapati, 2013. A modeling study of air migration from a drilling well to the surrounding aquifer in Appalachia. *World Environmental & Water Resources Congress*, Cincinnati, Ohio, USA.

Xiaolong Geng, Michel C. Boufadel, and A. Abdollahi-Nasab, 2013. Hydrodynamics in a sandy beach polluted with the Deepwater Horizon oil spill. *World Environmental & Water Resources Congress*, Cincinnati, Ohio, USA.

Xiaolong Geng, Hailong Li, and Yuqiang Xia, 2007. Tide-induced head fluctuations in a coastal aquifer: Effects of the elastic storage and leakage of the sediment on the seafloor. In: Proceeding of the International Professionals for the Advancement of Chinese Earth Sciences (IPACES) 6th Annual Meeting, Wuhan, China. Published by Journal of China University of Geosciences, Vol.18, Special Issue, p133-135.

A. Abdollahi-Nasab, Michel C. Boufadel, and **Xiaolong Geng**, 2013. Role of freshwater in the persistence of the Exxon Valdez oil spill in a wave-exposed beach. *World Environmental & Water Resources Congress*, Cincinnati, Ohio, USA.

Jagadish Torlapati, **Xiaolong Geng**, Tom King, Michel C. Boufadel, and Kenneth Lee, 2014. Shoreline Bioremediation Model (SBM) – A Graphical User Interface for Simulating the Biodegradation of Beached Oil, *International Oil Spill Conference*, Savannah, Georgia, USA (accepted).

To my Mother, Dingyu Hua

感谢妈妈，丁玉华

To Wangwang, to my aunts, Yuqin Ding and Yaqing Ding

感谢旺旺，感谢二姨，丁玉琴，老姨，丁亚青

ACKNOWLEDGMENT

First and foremost, I present my sincerest gratitude to Dr. Michel C. Boufadel, my research advisor, who greatly supported me throughout my PhD studies with his patience and knowledge. I am very grateful to the members of my doctoral dissertation committee: Dr. Nancy L. Jackson, Dr. Robert Dresnack, Dr. Lisa B. Axe, and Dr. Wen Zhang who generously gave their precious time and expertise to read and better my work.

Special thanks go to the staff in Natural Resources Development and Protection (NRDP). I am very grateful to their help and support.

I owe all my accomplishments to my truly exceptional family; to my mother and my aunts. There has not been a single moment in my life without their conditional support and desire for my success. Words are not able to express my gratitude to them.

Dr. Hailong Li, my master advisor, and his wife, Ms. Xinglin Li, are thoughtfully remembered. During the past years, they gave me great help and support.

The faculty and staff of Civil and Environmental Engineering Department and the administrative staff at the Graduate Office at Temple University and New Jersey Institute of Technology are gratefully recognized.

TABLE OF CONTENTS

TABLE OF CONTENTS
(Continued)

TABLE OF CONTENTS
(Continued)

Chapter **Page**

LIST OF TABLES

LIST OF FIGURES

LIST OF FIGURES
(Continued)

Figure **Page**

LIST OF FIGURES
(Continued)

LIST OF FIGURES
(Continued)

Figure **Page**

GLOSSARY

Flow-averaged approach: Net flow rate along the swash zone is estimated over one wave period, which is then set as the inflow boundary condition on the swash zone to drive the groundwater flow model.

Phase-averaged approach: Sea level oscillations are averaged over one wave period to generate phase-averaged sea levels, which are then set as the boundary condition on the aquifer-ocean interface to drive the groundwater flow model.

Phase-resolving approach: Sea level oscillations are directly set as the boundary condition on the aquifer-ocean interface to drive the groundwater flow model.

Specific humidity: A ratio of the water vapor content of the mixture to the total air content on a mass basis.

Surf zone: The region extending from the seaward boundary of wave breaking to the limit of wave uprush.

Swash zone: The part of the beach extending from a near-shore shallow depth to the limit of maximum inundation.

Vadose zone: The part of Earth between the land surface and the top of the phreatic zone i.e. the position at which the groundwater s at atmospheric pressure.

Wave breaking: A wave whose amplitude reaches a critical level at which some process can suddenly start to occur that causes large amount of wave energy to be transformed into turbulent kinetic energy.

Wave run-up: Maximum elevation of the waterline above the undisturbed water level.

Wave run-down: Minimum elevation of the waterline above the undisturbed water level.

CHAPTER 1

INTRODUCTION

1.1 Impacts of Waves and Evaporation on Coastal Groundwater Systems

Groundwater is an important resource impacting the structure and productivity of near-shore coastal ecosystems (Hancock et al., 2005; Michael et al., 2005). Managing it requires quantification of major factors affecting its spatial and temporal variation. Numerous studies have been conducted to evaluate the safe yield of groundwater wells subject to the stressors of population growth and sea level rise. These stressors tend to increase seawater intrusion into the groundwater. Soil water salinization has been recognized as a severe problem degrading the environment of coastal regions. While the majority of studies have focused on saltwater intrusion, the roles of waves and evaporation have not been considered in groundwater management of coastal aquifers. However, waves play an important role in the exchange of fluxes between the open water and the groundwater (Longuet-Higgins, 1983; Xin et al., 2010). Evaporation extracts water from the soil surface leaving the salt behind, which increases the pore water salinity, especially in regions with shallow groundwater tables (Nassar and Horton, 1989; Zarei et al., 2009; Liu et al., 2013). Subsequent oceanic forcing, such as tides and waves, may wash this zone and further alter subsurface solute distribution in the coastal aquifers. Therefore, quantification of evaporation affecting subsurface flow pattern and solute fate is critical for proper assessment and management of coastal groundwater resources.

There are numerous processes generating waves; this paper focuses on those generated by wind. Their periods are usually less than 10 seconds. Waves usually have extremely high frequency with small amplitudes. As the waves approach the coast, it enters

into shallow waters, which is known as shoaling. The subsequent wave breaking, and run-up and run-down, result in wave-energy dissipation onto the swash zone of the beach. The movement of waves affects the pattern of groundwater flow and associated solute transport in coastal aquifers (Longuet-Higgins, 1983; Baldock and Hughes, 2006; Sous et al., 2013). Therefore, understanding wave effects on groundwater flow and subsurface solute transport is very important for solving coastal environmental issues such as submarine groundwater discharge (Xin et al., 2010), transport of contaminants to the ocean (Kersten et al., 2005; Robinson et al., 2006), bioremediation of oil spills (Santas and Santas, 2000), and tsunami prevention (Goseberg et al., 2013).

Evaporation processes have been noted to occur in three stages (Menziani et al., 1999; Zarei et al., 2009). The first stage, named constant-rate or potential evaporation, is characterized by a constant evaporation rate controlled by external meteorological conditions such as radiation, wind speed, air temperature and humidity. The second stage is characterized by a falling evaporation rate below the potential rate. In this stage, the evaporation rate is limited by soil conditions (soil water content, matric potential gradient, hydraulic diffusivity), which determines the rate at which the soil can release moisture towards the surface. The third stage is established after the surface zone becomes dry such that further conduction of liquid water through it effectively stops.

1.2 Modeling Groundwater Flow and Solute Transport in Coastal Aquifers Subjected to Waves and Evaporation

The numerical modeling of waves combined with tidal forcing is computationally cost prohibitive, because the hydrodynamic model would require very small time steps and very fine meshes to resolve each phase. The groundwater flow model using waves as boundary

conditions would also require small time steps, but they could be larger than those used in the hydrodynamic model as the groundwater flow equations are dissipatives while nonlinear nature of the hydrodynamic flow equation could magnify errors. Xin et al. (2010) developed a phase-averaged approach to simulate groundwater flow and solute fate in coastal beaches subjected to wave forcing or combined wave and tide forcing. They averaged sea-level oscillations in one wave period and used them as boundary conditions in the variably saturated groundwater flow model SUTRA to simulate wave forcing affecting a subterranean estuary. Their results demonstrated that high-frequency waves induced pore water circulations in the near-shore zone of the coastal aquifers, while the combined wave and tide forcing intensified this flow circulation and shifted the freshwater discharge zone seaward. Further investigation was suggested in their study on the fate of land-sourced chemicals in the subterranean estuary subjected to different oceanic forcing. Bakhtyar et al. (2012c) conducted a comprehensive numerical study to investigate the transport of a solute plume in an unconfined coastal aquifer subjected to high and low frequency oceanic forcing. In their study, fluid motion in the ocean was simulated using the Reynolds-Averaged Navier-Stokes (RANS) equations; groundwater flow and solute transport were simulated using the model SEAWAT. Their results further demonstrated that oceanic fluctuations increased the residence time and dispersion of the plume; as the effects of tides and waves induced the formation of an upper saline plume beneath the beach face and were additive, both wave and tidal effects should be accounted for.

Most previous studies on wave effect modeling were based on saturated groundwater flow models (Li and Barry, 2000; Li et al., 2002; Bakhtyar et al., 2009; Bakhtyar et al., 2012a). But using saturated-flow models, the water table becomes an

impermeable boundary for water flow and solute transport, which is not realistic; while, in variably saturated models, the water table is simply the location where the water pressure is zero, a mathematical definition, and water and solute can traverse downward and upward (Boufadel et al., 1999a; Boufadel, 2000; Boufadel et al., 2011). Many studies have found that waves cause an extensive infiltration/exfiltration along the swash zone of the beach and capillary effects need to be accounted for in predicting wave-induced groundwater fluctuations in coastal beaches (Li et al., 1997; Horn, 2006). Therefore, there is a motivation to use a variably saturated flow model to simulate the responses of groundwater flow and associated solute transport to wave-included oceanic forcing.

Evaporation over bare ground soil involves very complex water vapor exchange between the soil surface and the atmosphere. Numerous schemes have been proposed to parameterize the evaporation process at the soil-atmospheric interface. They can be classified into two categories. In the first category, the estimation of evaporation rate is based on the maximum flux that the soil could supply or the potential rate the atmosphere would demand (Mahrt and Ek, 1984; Wetzel and Chang, 1987; Chattopadhyay and Hulme, 1997; Zarei et al., 2009), and the interaction between soil moisture and atmospheric conditions is ignored. The second category is the so-called “bulk aerodynamic method” (Mahfouf and Noilhan, 1991; Vandegriend and Owe, 1994; Mahrt, 1996), which provides an explicit relation between the evaporation flux at the soil surface and the near-surface water content. Within this category, specification of surface specific humidity is required to estimate evaporation rate from the soil surface. Evidently, coupling these formulations to groundwater flow and solute transport models enables more accurate evaluation of evaporation affecting groundwater flow patterns and solute transport process in soil.

Yakirevich et al. (1997) presented a one-dimensional model of water flow, heat, and salt transfer to investigate transient evaporation from bare saline soils. Their results demonstrated that the salt concentration gradient reduces evaporation from soil. Il'Ichev et al. (2008) developed a model to reveal instability of the salinity profile (salt fingering) during evaporation of saline groundwater. In their model, a concept of sharp evaporation-precipitation front was introduced to separate regions of soil saturated with an air-vapor mixture and with saline water. Appling their findings to realistic parameter regimes, they predicted that salt fingering is unlikely to occur in low-permeability soils, but is likely in high-permeability (sandy) soils under conditions of relatively low evaporative upflow.

The numerical models used in previous studies do not account for solute density effect on groundwater flow during evaporation. Moreover, most of these models are one-dimensional, which might not represent accurately groundwater dynamics and flow patterns during evaporation; previous studies have noted the formation of high salinity finger plume at the edge of dry lakes (Elder, 1967; Wooding et al., 1997; Boufadel et al., 1999b). Therefore, there is a motivation to adopt a two-dimensional density-dependent groundwater model to investigate the influences of evaporation on subsurface flow pattern and associated solute fates. A three-dimensional model could be considered in future work. But this work uses only a two-dimensional approach.

1.3 Objective

The objective of our work is to investigate wind waves and evaporation as two physical factors affecting the hydrodynamics of coastal aquifers. The investigation is carried out

through two parts. The first one investigates the effects of waves on groundwater flow and solute fate in coastal aquifers. A previous experimental study conducted by Boufadel et al. (2007) on a laboratory beach was used to provide information on movement of dissolved nutrients in subsurface flow due to the effects of waves. Numerical simulations were conducted against experiment data to quantify wave effects on groundwater flow and subsurface solute transport. The second part investigates evaporation effects on coastal groundwater systems. A field study complemented with numerical simulations was performed to quantify this effect. The main contributions of this investigation are as follows:

1. It reveals how wave forcing impacts solute fate in a laboratory beach prior to discharge into the sea, such as solute pathways, residence time, spreading, discharge rate, and discharge zone of the beach.

2. To address the exorbitant cost of conducting the simulation of waves, a new approach is developed to capture the essence of wave motion on beaches. The approach allows one to use much larger time steps in the groundwater flow models (around 100 times larger than that used in the hydrodynamic model).

3. Compare different effects of oceanic forcing, such as waves, tides, and combined waves and tides, on the injected solute fate in coastal aquifers.

4. Reveal how evaporation impacts groundwater flow and subsurface solute distribution.

5. Evaluate how soil characteristics, such as permeability and capillarity, affect subsurface solute distribution during evaporation.

CHAPTER 2

NUMERICAL STUDY OF WAVE EFFECTS ON GROUNDWATER FLOW AND SOLUTE TRANSPORT IN A LABORATORY BEACH

2.1 Abstract

A numerical study was undertaken to investigate the effects of waves on groundwater flow and associated subsurface solute transport based on tracer experiments in a laboratory beach. A 2-D unsaturated groundwater flow model MARUN was used to simulate the density-dependent groundwater flow and subsurface solute transport in the beach subjected to waves. Wave motion was simulated by means of Computational Fluid Dynamics (CFD) software, Fluent in two-dimensions, to provide seaward boundary conditions for the MARUN model. A case without wave forcing was also simulated for comparison. Simulation results generally matched the experimental data. The results revealed that waves induced seawater-groundwater circulations in the swash zone of the beach, which formed an upper mixing plume beneath the beach surface. In contrast to the no-wave case, wave forcing significantly affected the solute transport's pathways, residence time, and movement speed in the beach. Wave forcing also shifted the solute discharge zone further seaward. Spatial distribution of the inflow and outflow rates across the beach face indicated that the wave forcing formed a large seawater-groundwater interaction zone along the swash and surf zones of the beach. The results also suggested that the wave–induced seawater infiltration in the swash zone of the beach drove more solute downwards to the saturated zone of the beach, and subsequently decreased the proportion of the solute mass in vadose zone. This effect has implications on biochemical activities in the beach.

2.2 Introduction

In the last two decades, studies have revealed the groundwater system near the coastline is an important transport pathway for pollutants to enter the marine environment (Moore, 1996; Santas and Santas, 2000; Boufadel et al., 2007; Xin et al., 2010; Bakhtyar et al., 2012a). The near-shore groundwater system can be affected by many factors, such as tides (Guo et al., 2010; Bobo et al., 2012), waves (Nielsen, 1999; Boufadel et al., 2007), and water withdrawal through pumping and sea level rise (Calow et al., 1997; Alley et al., 2002). Gravity waves, can affect beach groundwater circulation patterns, and subsequently influence solute transport in near-shore aquifers (Bradshaw, 1974; Horn et al., 1998; Boufadel et al., 2007).

Experimental studies (Longuet-Higgins, 1983; Baldock and Hughes, 2006; Boufadel et al., 2007; Sous et al., 2013) and numerical studies (Turner and Masselink, 1998; Li and Barry, 2000; Li et al., 2002; Bakhtyar et al., 2012b) have demonstrated the effects of waves on hydrodynamics in near-shore aquifers. Experimental studies are usually carried out to reveal wave-related hydrodynamic phenomena in coastal aquifer systems. Longuet-Higgins (1983) provided an experimental illustration of wave effects on groundwater flow in the surf zone based on experiments conducted on a laboratory beach. He reported that waves approaching a sloping beach induced a tilt (wave set-up) in the mean water level within the surf zone. This wave set-up helped to drive an offshore bottom groundwater circulation in the beach. The earliest experimental study to quantify groundwater flow and solute transport in response to waves and tides was conducted by Boufadel et al. (2007). They performed tracer studies on a laboratory beach to study subsurface pollutant mixing and transport processes under the influences of waves. They

also observed that waves created a steep hydraulic gradient in the swash zone and a mild one landward of it; waves also created additional pathways for the tracer plume discharge across the beach surface and subsequently increased its residence time in the beach. In their study, the additional pathways were noted at a relatively deep conductivity meter (CM), where the tracer concentration reached high values for the wave case, while it remained at the background concentration in the absence of waves. Sous et al. (2013) studied groundwater circulation and percolation (through-bed) flows in a sandy laboratory beach in response to wave forcing. Their experimental results showed that in the swash zone, the main tendency is downward infiltration flow; flow exfiltration was not observed during the uprush-backwash cycle. Seaward of the swash zone on the beach surface, cycles of infiltration-exfiltration were observed in response to free surface waves.

Numerical models were also developed to better understand the effects of wave forcing on groundwater flow and associated subsurface solute transport in coastal beaches. Li et al. (1997) developed a modified kinematic boundary condition approach to represent high-frequency water table fluctuations due to wave run-up. Their simulation results showed similar features of water table fluctuations observed in the field. However, associated solute transport was not considered in their study. Xin et al. (2010) presented a numerical model to examine and quantify the individual and combined effects of waves and tides on groundwater flow and salt transport in near-shore aquifer systems. They simulated density-dependent flow in the beach groundwater system by coupling a near-shore wave model BeachWin and a variable density flow model SUTRA. The modeling results demonstrated a wave-generated onshore tilt in phase-averaged sea level; the resulting hydraulic gradient induced groundwater flow circulations in the near-shore

zone of the coastal aquifers and subsequently formed an upper saline plume similar to that formed due to tides. Bakhtyar et al. (2012b) also investigated transport of variable-density solute plumes in beach aquifers subject to tidal and wave forcing. In their paper, fluid motion in the ocean was simulated using the Reynolds-Averaged Navier-Stokes (RANS) equations; variable-density groundwater flow and solute transport in a near-shore beach subject to oceanic forcing were simulated using SEAWAT. Their simulation results confirmed that forcing due to tide and waves induced an upper saline plume in the beach. The results further demonstrated the effect of wave and/or tidal forcing on the solute plume's pathways, residence time and discharge rate across the beach face.

Most previous modeling studies are based on numerical experiments using saturated groundwater flow models (Li and Barry, 2000; Li et al., 2002; Bakhtyar et al., 2009; Bakhtyar et al., 2012a; Bakhtyar et al., 2012b). Studies have found that in saturated flow models, the water table becomes an impermeable boundary for water flow and solute transport, which is not realistic; in variably saturated models, the water table is merely the locus of points where the water pressure is zero, and thus water and solute can traverse it both downward and upward (Boufadel et al., 1999a; Boufadel, 2000; Boufadel et al., 2011). Therefore, there is a motivation to use a variably saturated flow model to simulate the responses of groundwater flow and transport characteristics to waves based on laboratory experiments.

2.3 Experiments and Methodologies

2.3.1 Experiments

A previous experimental study conducted by Boufadel et al. (2007) on a laboratory beach was used to provide information on movement of dissolved nutrients in subsurface flow due to wave effects. The experiments were performed in a carbon steel tank (8 m long × 2 m high × 0.6 m wide). To enable visual observations of the experimental results, one of the long walls of the tank was made of transparent plexiglass sheets. Sand was placed in the tank with a total horizontal length of 6.3 m at the base. A beach was built with a slope of 10% between 0 m and 5 m distance, and a 30% slope between 5 m and 6.3 m distance (Figure 2.1).

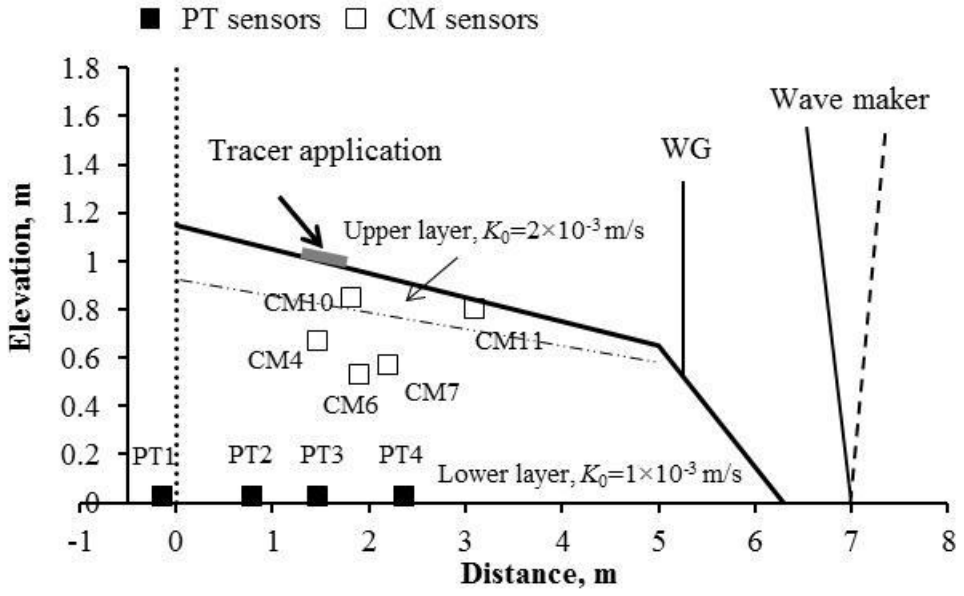

Figure 2.1 Experimental beach setup showing conductivity meters (CMs), pressure transducers (PTs), water gauge (WG), and wave maker.

Beach material consisted of coarse sand with a median size of 1 mm and a particle size distribution varying from 0.8 mm to 1.2 mm. The porosity of the sand was 0.33. The saturated hydraulic conductivity was 2×10^{-3} m/s, and the values of van Genuchten (1980) unsaturated parameters were $\alpha = 15.5$ m^{-1} and $n = 3.5$. These parameters were estimated by Boufadel et al. (1998a) using a Bayesian approach. The open water level in the tank was measured using a wave gauge (WG, Model NO. LV5900, Omega Engineering) as shown in Figure 2.1. Four pressure transducers (PT, Model NO. 1151AP, Fisher) were deployed at 3 cm above the bottom of the tank to measure water pressure in the beach. Ten conductivity meter sensors (CM, CDCN 108, Omega Engineering) were placed at different locations of the beach to measure salt concentrations. Locations of WG, PTs and CMs are given in Table 2.1.

Table 2.1 Location of Pressure Transducers, Water Gauge, and Conductivity Meters

Sensor	*x* (m)	*z* (m)	*y* (m)
PT1[a]	-0.15	0.03	0.6
PT2	0.78	0.03	0.6
PT3	1.47	0.03	0.6
PT4	2.355	0.03	0.6
WG	5.2	NA	0.3
CM4	1.47	0.67	0.15
CM6	1.9	0.53	0.3
CM7	2.2	0.57	0.5
CM10	1.81	0.85	0.1
CM11	3.1	0.8	0.2

Note: *x* = horizontal distance from the screen (positive seaward); *z* = elevation from the bottom of the tank; *y* = horizontal depth from the plexiglass wall (positive inward perpendicular to the plan of Fig.1). "NA" denotes that data are not applicable.
[a]The sensor is landward of the screen.

Two experiments with and without wave effects were performed in Boufadel et al. (2007). The tank was filled with tap water which had a background ion concentration of 0.15 g/L. The water level at landward of the beach (PT1 in Figure 2.1) was fixed at 1.0 m and the seaward water level (WG in Figure 2.1) was fixed at 0.9 m. The levels were relative to the bottom of the tank. After the beach approached a steady state hydraulic regime, 100 L of NaCl solution with concentration of 2.76 g/L was applied onto the beach surface for both experiments with and without wave effects, at location of approximately between x = 1.25 m and x = 1.50 m. The duration of the tracer application was about 50 min. Wave generation was started immediately after the tracer application by the rotation of an eccentric flywheel. Height and period of the waves were 4.8 cm and 1.11 s, respectively.

2.3.2 Methodologies of the Numerical Model

2.3.2.1 MARUN Model. Numerical simulations were conducted using the MARUN (MARine UNsaturated) model, which can simulate density-dependent flow and solute transport in variably saturated porous media (Boufadel et al., 1999a; Boufadel, 2000). The equation for the conservation of water can be written as:

$$\beta\phi\frac{\partial S}{\partial t}+\beta S_0 S\frac{\partial \psi}{\partial t}+\phi S\frac{\partial \beta}{\partial t}=\frac{\partial\left(\beta\delta K_x\frac{\partial \psi}{\partial x}\right)}{\partial x}+\frac{\partial\left(\beta\delta K_z\frac{\partial \psi}{\partial z}\right)}{\partial z}+\frac{\partial(\beta^2\delta K_z)}{\partial z} \qquad (2.1)$$

where β is the density ratio [-] defined as ρ/ρ_0 and δ is the dynamic viscosity ratio [-] defined as μ_0/μ; ρ and ρ_0 are salt-dependent water density [ML^{-3}] and freshwater density [ML^{-3}], respectively; μ_0 and μ are freshwater dynamic viscosity [$ML^{-1}T^{-1}$] and salt-dependent water dynamic viscosity [$ML^{-1}T^{-1}$]; ϕ is the porosity of the porous medium

[-], S is the soil moisture ratio [-], S_0 is the specific storage [L^{-1}], ψ is the pressure head [L], and K_x and K_z are the horizontal and vertical freshwater hydraulic conductivities [LT^{-1}].

Soil moisture ratio S and freshwater hydraulic conductivities K are correlated by the van Genuchten (1980) model, which have the expressions as

For $\psi \geq 0$, S =1.0, $K_x = K_{xo}$, $K_z = K_{zo}$, (2.2)

where K_{xo} and K_{zo} are the saturated horizontal and vertical freshwater hydraulic conductivities, respectively.

For $\psi < 0$, the effective saturation ratio S_e is given by:

$$S_e = \frac{S - S_r}{1 - S_r} = [\frac{1}{1 + (\alpha |\psi|)^n}]^m, \quad (2.3)$$

and K_x and K_z are given by

$$S_e = \frac{S - S_r}{1 - S_r} = [\frac{1}{1 + (\alpha |\psi|)^n}]^m, \quad (2.3)$$

$$K_j = K_{jo} S_e^{(1/2)} [1 - (1 - S_e^{1/m})^m]^2, \quad (2.4)$$

where $j = (x, z)$, $m = 1 - (1/n)$, S_r is the residual saturation ratio, and $|\psi|$ is the absolute value of ψ.

Following Boufadel et al. (1999a) and Boufadel (2000), the solute transport equation (convection-dispersion equation) can be written as:

$$\phi S \frac{\partial c}{\partial t} = \beta \nabla \cdot (\phi S D \cdot \nabla c) - \mathbf{q} \cdot \nabla c, \quad (2.5)$$

where c is the solute salt concentration [M L^3]. Darcy flux vector **q** is given by:

$$\mathbf{q} = (q_x, q_z) = -K_i \delta \left(\frac{\partial \psi}{\partial x}, \frac{\partial \psi}{\partial z} + \beta \right), \; i = (x, z). \tag{2.6}$$

The term D represents the physical dispersion tensor written as:

$$D = \frac{1}{\| \mathbf{q} \|} \begin{pmatrix} \alpha_L q_x^2 + \alpha_T q_z^2 & (\alpha_L - \alpha_T) q_x q_z \\ (\alpha_L - \alpha_T) q_x q_z & \alpha_T q_x^2 + \alpha_L q_z^2 \end{pmatrix}, \tag{2.7}$$

where $\| \mathbf{q} \| = \sqrt{q_x^2 + q_z^2}$, α_L and α_T are the longitudinal and transverse dispersivities [L], respectively.

2.3.2.2 Boundary and Initial Condition. In the landward boundary, as the water table was fixed and no solute leaves or enters the domain by diffusion at the boundary, a Dirichlet boundary condition and zero dispersion flux Neumann boundary were applied for water flow and solute transport, respectively. In the seaward boundary, the no-flow and zero dispersion flux boundary condition ($\partial \psi / \partial n = 0$ and $\partial c / \partial n = 0$) were used on the beach surface above the water level. Below the water level, boundary conditions of the simulation of solute transport followed the rule of "outflow boundary condition". In other words, if water enters the domain, a Dirichlet boundary was used which means that the concentration in the boundary is equal to that of the open water; if the solute leaves the domain, a Neumann boundary was assigned with zero dispersion flux. The Dirichlet boundary condition can be expressed as:

$$\psi(\mathrm{x}, \mathrm{z}) = \mathrm{H}_{Total} - \mathrm{z}(1 + \varepsilon \, \mathrm{c}_{sea}), \tag{2.8}$$

where H_{Total} is the total head. For no-wave case, H_{Total} was equal to the still water level. For wave case, H_{Total} is generated at each time step by using VOF multiphase model (wave motion simulator). The hydrodynamic model was based on solving the RANS equations, on the platform of Fluent software, to predict fluid motion in open water (Hirt and Nichols, 1981). The model adopted the Volume of Fluid (VOF) method to track the movement of the water surface, and the turbulence closure module k-ε, where k is the kinetic energy due to turbulence and ε is the rate of dissipation of k ($\varepsilon = \partial k / \partial t$).

In the tracer application segment (~25 cm), a flux (Neumann) boundary condition was used whose value was obtained as follows. The applied flow rate covered the width (60 cm) of the tank and 25 cm in the seaward direction. Because the model is two-dimensional (a vertical slice), the flux per unit width of tank (~5.0×10^{-5} m^2/s) was adopted, while the injection concentration of 2.76 g/L was assigned to the boundary as a Dirichlet boundary condition. Before and after the tracer application period, the no-flow and zero dispersion flux Neumann boundary condition were applied.

2.3.2.3 Numerical Implementation. A mesh of 106 nodes in the horizontal and 58 nodes in the vertical directions was employed in the domain, which gave a total of 6148 nodes, and 11970 triangular elements. Mesh resolutions were 0.06 m horizontally and 0.02 m vertically. The model was first run for 10-hour simulations without tracer application until the hydraulic regime reached a steady state; then, the simulation results were used as initial condition for the simulation of tracer application of which the simulation continued to another 5 hours. A very small time step (0.01 s) was chosen for the simulation of the wave case. Calibrated model parameters based on simulation results are summarized in Table 2.2.

Table 2.2 Model Parameter Values Used in the Numerical Simulations

Symbol	Definition	Units	Value
α	Sand capillary fringe parameter of the van Genuchten [1980] model	$1m^{-1}$	15.5
n	Sand grain size distribution parameter of the van Genuchten [1980] model	-	3.5
K_0	Saturated freshwater hydraulic conductivity	ms^{-1}	2.0×10^{-3} (Upper layer) 1.0×10^{-3} (Lower layer)
α_L	Longitudinal dispersivity	m	0.02
α_T	Transverse dispersivity	m	0.002
ε	Fitting parameter of density concentration relationship	lg^{-1}	7.44×10^{-4}
S_0	Specific storage	$1\ m^{-1}$	10^{-5}
S_r	Residual soil saturation	-	0.01
Φ	Porosity	-	0.33
CONVP	The convergence criterion of pressure head in the Picard iterative scheme of MARUN code	m	10^{-5}
τD_m	Product of tortuosity and diffusion coefficient	m^2s^{-1}	10^{-9}

2.4 Result and Discussion

2.4.1 Water Table

Modeling results for both wave and no-wave cases show a good agreement (errors are less than 1 cm) with observations revealing approximately the same water table at each PT. Therefore, only results of the wave case are presented in Figure 2.2. The water table at PT2, PT3, and PT4 abruptly increased at the beginning of the simulation and maintained a higher value during the first 50 minutes. The increase in elevation is due to the application of the tracer solution onto the beach. The temporal measurements at PTs in the beach demonstrated the following facts: (1) based on the general hydraulic gradient the hydraulic gradient was seaward. The application of tracer solution onto the beach did not greatly alter

the general hydraulic gradient, which implies that the injected plume in the beach will flow seaward; (2) the variation of water table at PTs is almost the same for both wave and no-wave cases, which indicates that the effect of wave forcing is negligible on the hydraulic regime at the lower part of the beach.

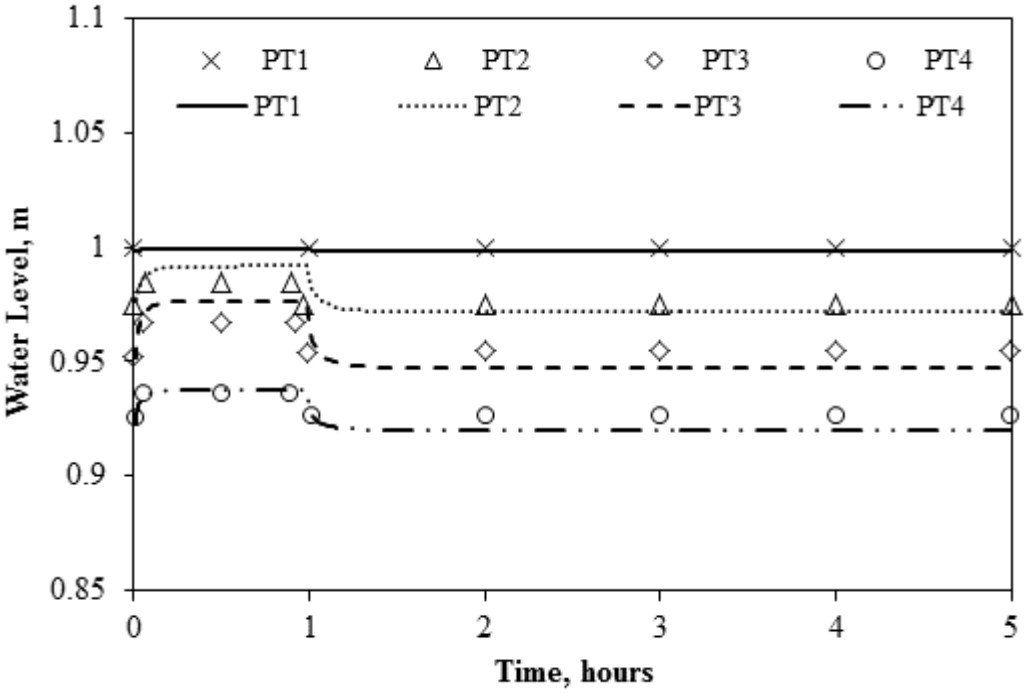

Figure 2.2 Observed (symbols) and simulated (curves) water levels at four PTs. Note that the sudden increase in beach water table is due to the application of tracer injection.

2.4.2 Salinity

Figures 2.3a-2.3e present the temporal variation of the salt concentrations at CMs. Discrepancies are observed between predicted and observed data, especially at CM4 and CM10. Reasons for these differences may be due to the following: (1) The CMs were encased in screened plexiglass boxes to avoid direct contacts with sand. The boxes were 10 cm × 10cm × 10 cm in dimension. Therefore, the observations depict an average value of

the sampling volume, while the simulation results represent the concentration at a single point location of CM; (2) local heterogeneity may exist in the tank, which could create different three-dimensional pathways for solute transport that are not accounted for in the two-dimensional model MARUN. Furthermore, for the wave case, the morphologic change of the beach profile due to wave forcing is not considered in the simulation, which may cause the differences between modeling results and observations.

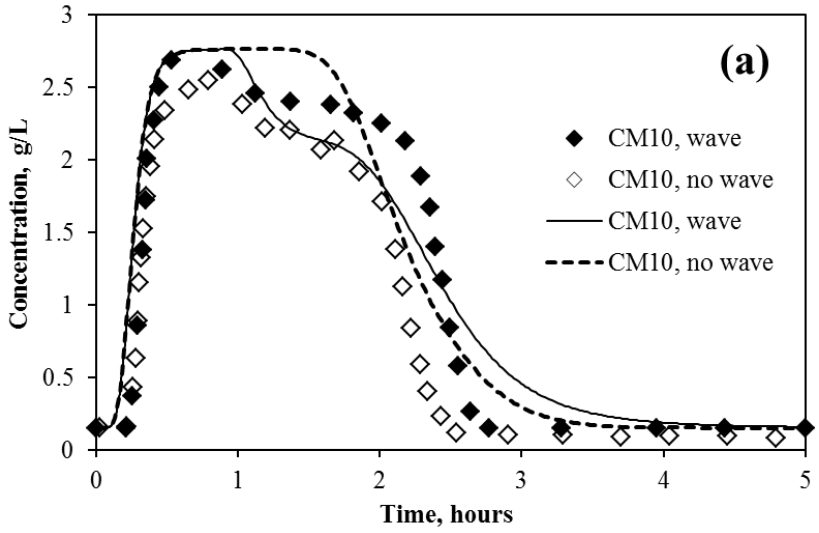

Figure 2.3 (a-e) Observed (symbols) and simulated (lines) concentrations at CMs for the wave and no-wave cases.

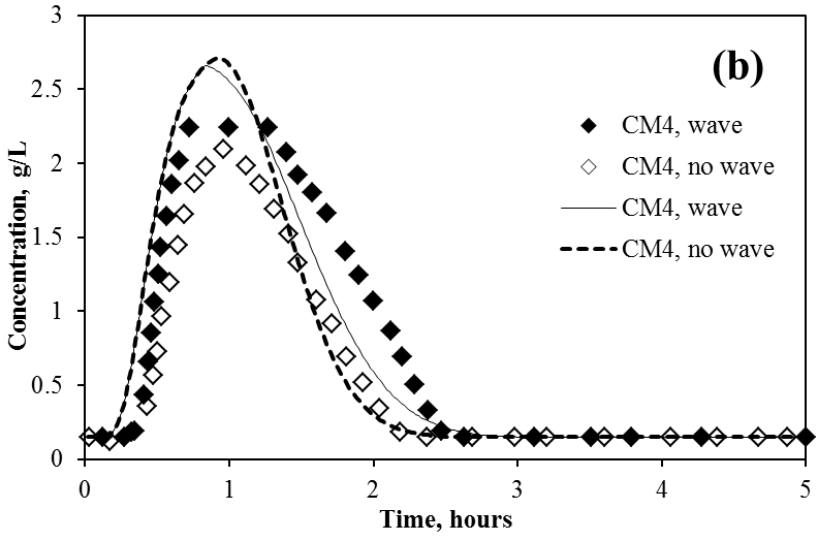

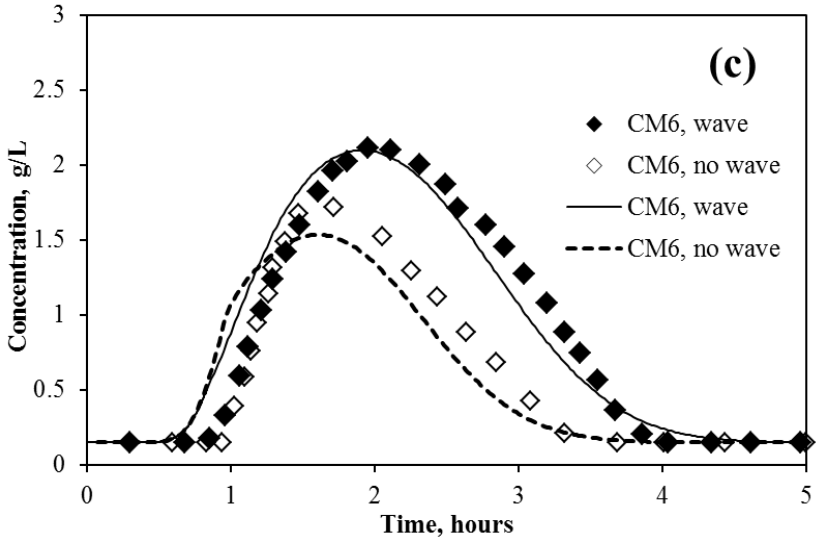

Figure 2.3 (a-e) Observed (symbols) and simulated (lines) concentrations at CMs for the wave and no-wave cases (continued).

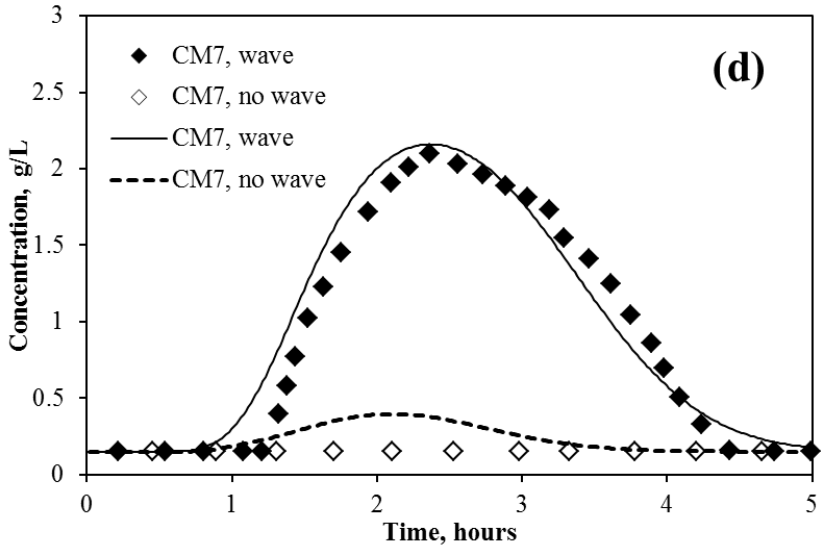

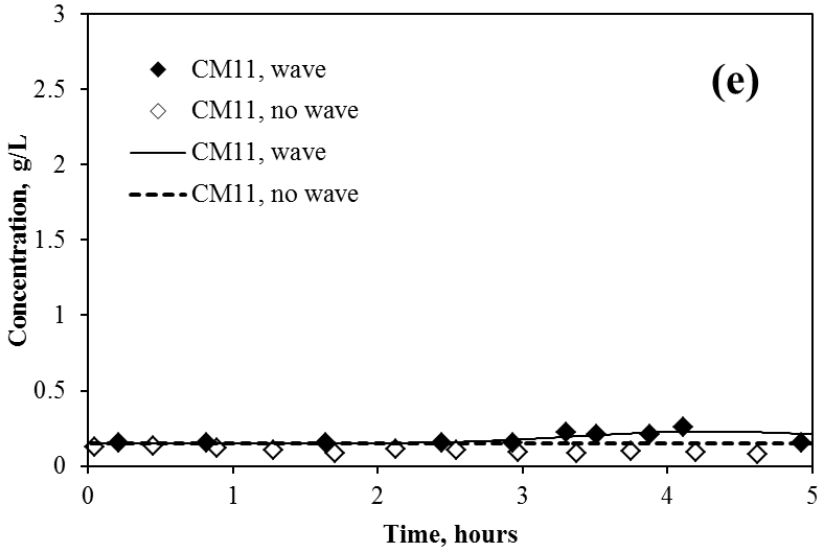

Figure 2.3 (a-e) Observed (symbols) and simulated (lines) concentrations at CMs for the wave and no-wave cases (continued).

Comparison of the salinity measurements at CMs for the two cases shows that the behavior of the solute migration in the beach was different under different conditions (with/without wave forcing). For the no-wave case, the concentrations started to increase at time t = 0.2 h at CM10, 0.3 h at CM4, 0.8 h at CM6, and 1.1 h at CM7, respectively. The

concentrations reached peaks of 2.2 g/L at CM4, 1.8 g/L at CM6, and 2.5 g/L at CM10, and remained at relatively high values for a duration of 2.5 hours at CM4 and CM10, and 3.0 hours at CM6. There was no obvious change in concentration at sensors CM7 and CM11. In the case of wave forcing, the rise time at sensors CM4, CM6, and CM10 is almost the same with the time for the no-wave case; however, the high concentration duration increased 20% at CM10 and CM4, and 14% at CM6. Moreover, there were pronounced differences in salinity measurements at sensors CM6 and CM7 between the two cases; the maximum concentration at sensor CM6 increased 28% (1.75 g/L for the no-wave case; 2.25 g/L for the wave case). That of CM7 increased 1,200% (0.15 g/L for the no-wave case; 2.0 g/L for the wave case). Compared to the no-wave case, the longer duration of relatively high concentration for the wave case indicates that the wave forcing increased the residence time of plume in the beach. Moreover, the different breakthrough curves at sensors CM6 and CM7 indicate that the waves modified the pathways of the plume migration in the beach.

2.4.3 Plume Motion

Figures 2.4a and 2.4b illustrate the plume movement for both wave and no-wave cases at different time. In the case of no wave forcing, the tracer plume was discharged from the beach surface near the water level line, which indicates that the solute migration is dominated by the local groundwater hydraulic gradient. The plume also showed a long tail in the unsaturated zone of the beach (above the groundwater table) after the tracer injection. This condition is most likely due to the lower hydraulic conductivity in the unsaturated zone of the beach (which is due to low soil moisture); migration of the solute plume in the unsaturated zone is slower than in the saturated zone. In the case of wave

forcing, during the first 50 minutes without wave implementation, the subsurface solute plume migrated seaward along the beach surface (shown in Figure 2.4b at time t = 0.5 h). When waves were acting on the beach, in the swash zone, the plume started to migrate deeper and around the upper freshwater plume, formed by the freshwater infiltrating the beach due to wave set-up and run-up; then, the plume discharged at the lower part of the beach face (shown in Figure 2.4b at time t = 1, 2, 3, 4, and 5 h). This behavior further confirmed that wave forcing modified the pathways of solute transport near the beach surface. The simulation results also demonstrate that wave forcing increases the residence time of the plume in the beach. After 5 hours of simulation, for the no-wave case, the injection-induced high salinity plume had totally discharged from the beach surface to the open water. For the wave case, the plume contour can still be observed in the beach (Figure 2.4b)

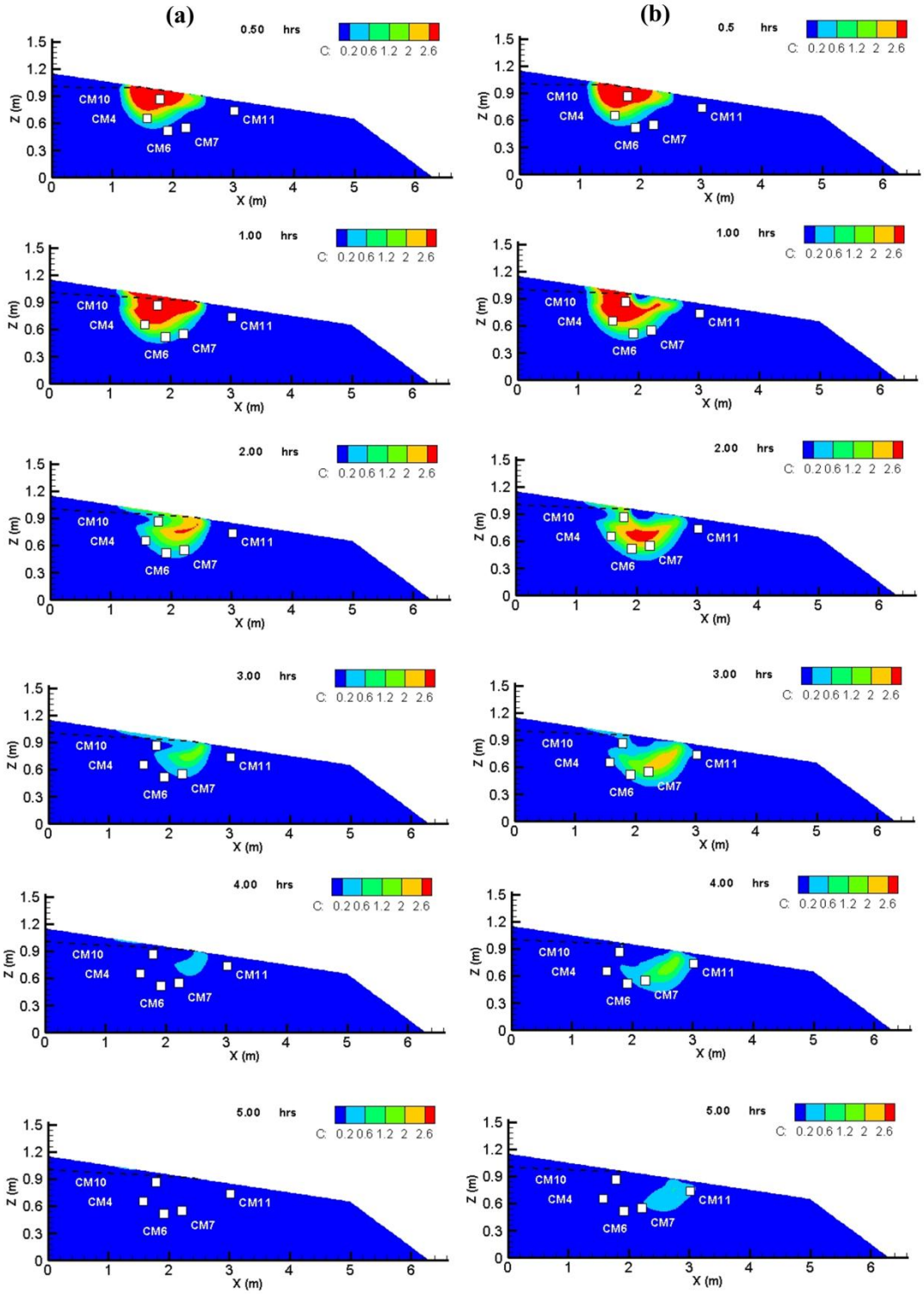

Figure 2.4 Concentration (in g/L) contours at different time along with groundwater table (dash line) for both the no-wave (a) and wave cases (b).

Figure 2.5a shows the trajectory of the plume centroid as a function of time for the wave and no-wave cases. In the first 50 minutes, the centroid of plume shows the same trajectory for both cases because waves were not generated during the high salinity solute application. However, the trajectory of the plume centroid shows a clear difference between the wave and no-wave cases when wave forcing was acting on the beach. Under wave forcing, the plume centroid migrated deeper and farther seaward before it discharged from the beach. The average speed of the plume centroid was calculated based on its trajectory length and travel time. The estimated values were 4.21 m/day and 3.17 m/day for the no-wave case and 5.65 m/day and 5.07 m/day for the wave case, including and excluding the first 50 minutes' injection, respectively. The calculation indicates that in addition to modifying the solute's trajectory and residence time, wave forcing also accelerated the movement of the solute in the beach. Figure 2.5b shows the variation of normalized mass (current divided by that at 50 minutes) of the solute in the beach as a function of time. For both cases, the normalized mass of the solute first increased due to the continuous high salinity solution application onto the beach and then decreased because the solute gradually discharged across the beach surface. After the injection, the mass of the solute remaining in the beach subjected was lower for a short period for the wave case in comparison to the no-wave case. This is due to the fact that the injection-generated high salinity plume was initially diluted by the upper freshwater plume, formed by wave-induced infiltration in the swash zone. The normalized solute mass was always higher in the wave case after the short period of initial dilution. Also, after 4 h, 2% of the solute remained in the beach in the no-wave case to be compared to 20% for the wave case. This temporal mass variation of solute in the beach indicates that waves affect the process

of subsurface solute discharge. Under wave forcing, the beach solute discharge will continue for a longer time at a relatively smaller rate.

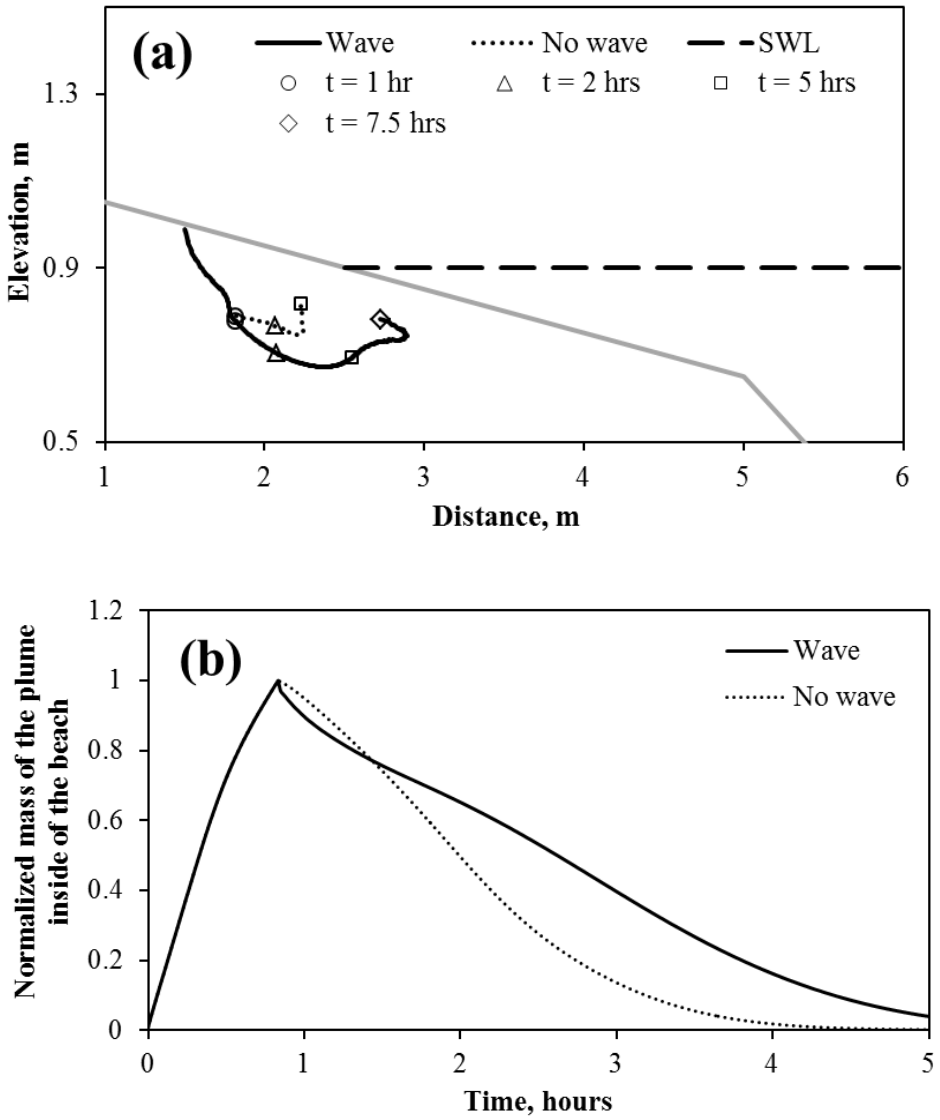

Figure 2.5 (a) Trajectories of the plume centroid in the beach for both the no-wave and wave cases. The locations of the plume centroid at specific time are shown as symbols; (b) Variation of normalized mass of the plume in the beach as a function of time. The mass of the plume is normalized by its maximum value which occurred 50 min after injection.

2.4.4 Groundwater Recirculation Rates

Figures 2.6a and 2.6b show the distribution of inflow and outflow rates across the beach face. These values were calculated by integrating the simulated fluxes over the

experimental period of no solute application onto the beach. In the case where no wave forcing was applied to the beach, the groundwater discharge is driven only by the global seawater hydraulic gradient (water level landward of the beach is higher than that of the sea). The discharge rate is largest at the interface of the beach surface and open water level, and sharply decreases to zero along the seaward direction of the beach. Under wave forcing, significant influx occurred in the upper region of the swash zone. This infiltration mixed with groundwater and discharged by seawater-groundwater circulation at the lower region of the swash zone (the base of the backwash zone). The groundwater discharge zone broadens both landward and seaward, while the location with the largest discharge rate shifts farther seaward. Meanwhile, larger groundwater exfiltration along with seawater infiltration occurred in that zone, indicating that high-frequency wave forcing induces groundwater-seawater circulation in the beach and subsequently increases beach flux exchange between groundwater and seawater. The exfiltration rate increased 500% due to wave forcing (2.55 $m^3day^{-1}m^{-1}$ for the no-wave case to 15.32 $m^3day^{-1}m^{-1}$ for the wave case). The infiltration rate for the wave case was 13.18 $m^3day^{-1}m^{-1}$. This large wave-induced flux exchange between seawater and groundwater would play a crucial role in nutrient biogeochemical cycles between subterranean estuary and coastal ocean, such as non-conservative behavior of dissolved Fe concentrations (Rouxel et al., 2008), cation exchange (Zghibi et al., 2012), pH and dissolved oxygen distribution (Robinson et al., 2007) and BTEX biodegradation in subterranean estuaries (Robinson et al., 2009).

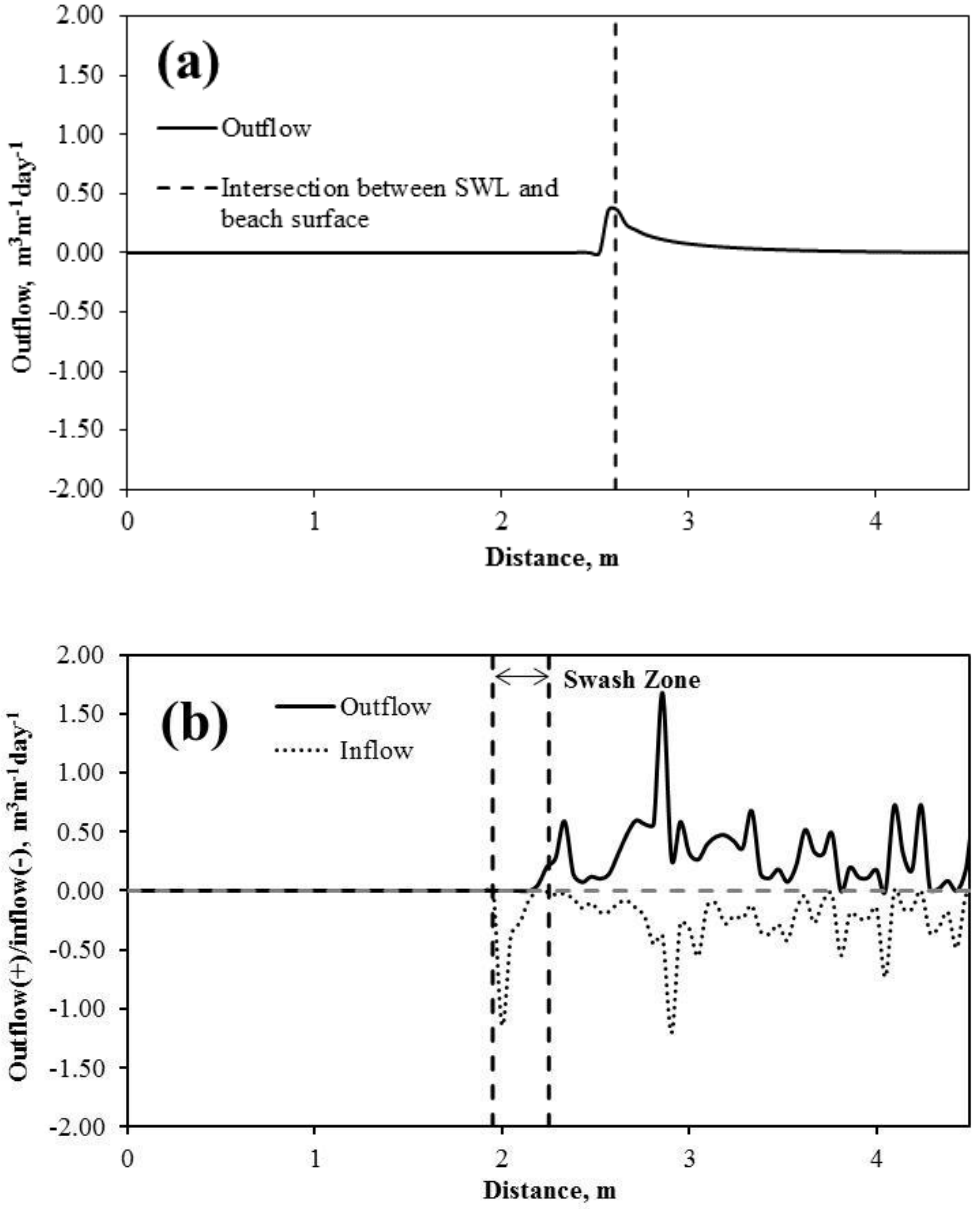

Figure 2.6 Distributions of the inflow and outflow rates across the beach-sea interface for no wave (a) and wave cases (b). The rate was calculated by integrating the simulated fluxes over the experimental period of no solute application onto the beach.

2.4.5 Plume in Vadose Zone

The temporal change of the plume mass in the vadose zone of the beach is shown in Figure 2.7. Note that the mass was normalized by its maximum value which occurred 50 min after

injection. In the absence of wave forcing, the normalized mass in the vadose zone first increased gradually to 0.04 until the end of injection (t = 0.83 h), and then it rose abruptly reaching its peak of 0.13 within 10 minutes. The gradual increase of the solute mass in the vadose zone along with the rise in the water table is due to the continuous injection of the high salinity solution into the beach. After injection, the water table elevation rapidly decreased to its initial condition (shown in Figure 2.2). This sudden decrease caused a certain amount of solute to remain above the water table in the beach, which increased the proportion of solute mass in the vadose zone. Therefore, the normalized mass curve shows an abrupt rise within a short period after injection. Under wave forcing, the change of the solute mass in the vadose zone reveals a similar trend but the proportion of solute mass in the vadose zone is much smaller. The reasons for these differences are as follows: the wave–induced freshwater infiltration in swash zone of the beach drove more solute downwards to the saturated zone of the beach, and subsequently decreased the proportion of the mass in the vadose zone. In addition, the infiltration in the swash zone due to waves narrowed the vadose zone of the beach and subsequently reduced the solute mass in the vadose zone. Therefore, the mass change of solute in the vadose zone of the beach suggests that in addition to affecting solute transport in the saturated zone, wave forcing also affects solute behavior in the unsaturated zone.

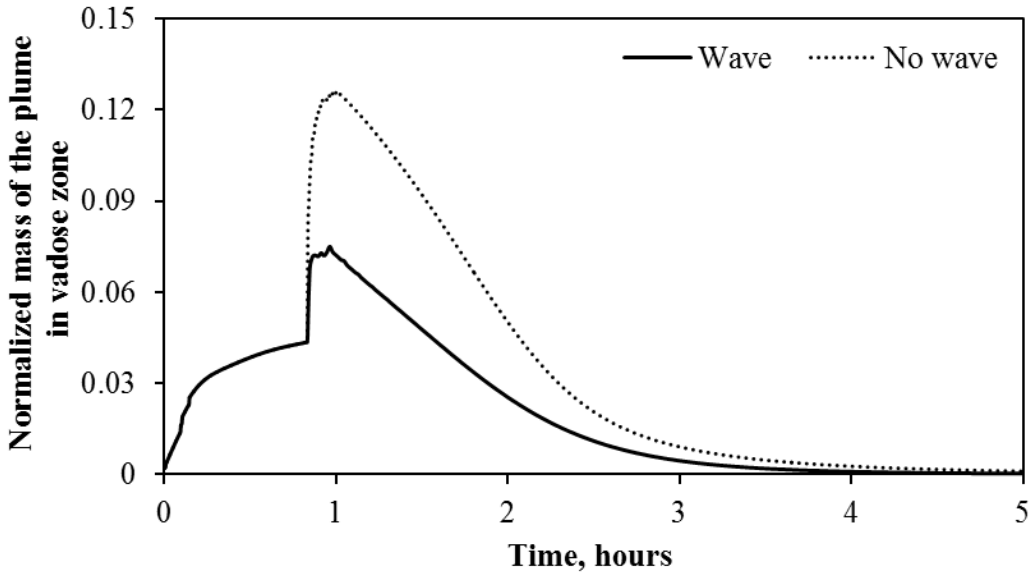

Figure 2.7 Variation of normalized mass of solute in the vadose zone as a function of time. The mass of the plume is normalized by its maximum value which occurred 50 min after injection.

2.5 Summary and Conclusions

High-frequency waves are an important oceanic forcing affecting groundwater flow and subsurface solute transport in coastal aquifers. Wave forcing induces groundwater-seawater circulation in the swash, causing the solute plume to migrate deeper and discharge farther seaward. This effect increases the trajectory length of subsurface solute transport and the residence time of the plume. Wave forcing also accelerates the speed of solute movement in the beach. Spatial distribution of the inflow and outflow rates across the beach face indicate that wave forcing significantly increases beach flux exchange between groundwater and seawater across the swash and surf zones of the beach. The results also suggest that wave–induced seawater infiltration in the swash zone increases the solute moving below the groundwater table and decreases the proportion of the solute mass in the vadose zone. In field conditions, wave forcing occurs with other

processes affecting near-shore groundwater systems, such as tides, buoyancy (due to presence of freshwater in a marine environment), pumping and climatic stresses. Therefore, further comprehensive studies are necessary to investigate the combined effects of these conditions on near-shore groundwater systems.

CHAPTER 3

NUMERICAL STUDY OF SOLUTE TRANSPORT IN SHALLOW AQUIFERS SUBJECTED TO WAVES AND TIDES

3.1 General

A numerical study was conducted to investigate the fate of solute in coastal beaches in response to high (waves) and low (tides) frequency oceanic forcing. A flow-averaged approach was developed to generalize wave motions acting onto the beach for the sake of the feasibility of numerical computation. A two-dimensional numerical model MARUN was used to simulate variably saturated, variably density groundwater flow, and subsurface solute transport in coastal aquifers. Seven scenarios were simulated to investigate wave forcing, tide forcing, and combined wave and tide forcing affecting injected solute fates in coastal groundwater systems. The plume's trajectory, residence time, migration speed, discharge zone, and discharge rate were quantified. The results suggested that wave forcing caused the plume to migrate deeper and discharge in the proximity of the water table's exit point of the beach, while tide forcing caused the plume to migrate along the beach face and discharge at low tide zone of the beach. The combined wave and tide forcing seems to have all the characteristics of each separate oceanic forcing affecting subsurface solute fates. Under the combined oceanic forcing condition, the plume was pushed deeper as it transported to the low tide zone of the beach. This effect elongated the trajectory length of solute transport and subsequently increased its residence time beneath the beach.

3.2 Numerical Experiment Implementations

3.2.1 Model Setup and Numerical Implementations

The model setup was based on laboratory beach experiments conducted in Boufadel et al. (2007) (Figure 2.1). The beach was 6.3 m long, 1.15 m high and 0.6 m wide. The beach has a slope of 10% between 0 m and 5 m distance, and a 50% slope between 5 m and 6.3 m distance. To investigate wave effects on groundwater flow and solute fates, Boufadel et al., (2007) conducted tracer studies in the beach subjected to waves. The application segment is 25 cm long between x=1.25 m and x = 1.5 m. A 100 L of NaCl solution at the concentration of 2.76 g/L was applied into the beach within 50 min, and then different oceanic forcing was acting onto the beach. The water table at landward of the beach was fixed at 1.0 m and still water level in open water was 0.9 m. The background salinity in the beach and open water is 0.15 g/L.

The numerical experiments conducted in this study followed the same laboratory experiment implementations performed in Boufadel et al., (2007) but with more scenario tests on oceanic forcing affecting groundwater flow and solute fates. Seven scenarios were simulated, where the beach was subjected to wave forcing (Scenario 1, 2, and 3), tide forcing (Scenario 4, 5, and 6), and combined wave and tide forcing (Scenario 7). The oceanic properties of the scenarios were summarized in Table 3.1. The parameter values used for the simulation, shown in Table 2.1, have been validated in previous modeling study (Boufadel et al., 2011).

Table 3.1 Properties of Oceanic Forcing (Waves and Tides) in the Numerical Experiments

Scenario	H (cm)	T_w (s)	Simulated Net in/exfiltration[1] ($m^3day^{-1}m^{-1}$)	
1	4.0	1.11	-0.91	
2	4.0	2	-1.91	
3	8.0	1.11	-1.78	
Scenario	A (m)	T_t (min)		
4	0.4	37.5		
5	0.3	37.5		
6	0.4	75		
Scenario	A (m)	T_t (min)	H (cm)	T_w (s)
7	0.4	37.5	4.0	1.11

[1]The negative value denotes infiltration, while positive value denotes exfiltration.

The domain was a two-dimensional representation of the beach (6.3 m long × 1.15 m high). A mesh of 106 nodes in the horizontal and 58 nodes in the vertical directions was employed in the domain, which gave a total of 6148 nodes, and 11970 triangular elements. Mesh resolutions were 0.06 m horizontally and 0.02 m vertically. In the landward boundary, as the water table was fixed and no solute leaves or enters the domain by diffusion at the boundary, a Dirichlet boundary condition and zero dispersion flux Neumann boundary were applied for water flow and solute transport, respectively. In the seaward boundary, the no-flow and zero dispersion flux boundary condition ($\partial\psi / \partial n = 0$ and $\partial c / \partial n = 0$) were used on the beach surface above the water level. Below the water level, boundary conditions of the simulation of solute transport followed the rule of "outflow boundary condition". In other words, if water enters the domain, a Dirichlet boundary was used which means that the concentration in the boundary is equal to that of

the open water; if the solute leaves the domain, a Neumann boundary was assigned with zero dispersion flux. The Dirichlet boundary condition can be expressed as:

$$\psi(x,z) = H_{Total} - z(1+\varepsilon c_{sea}), \tag{3.1}$$

where H_{Total} is the total head of water. Modeling of this sea level oscillation is elaborated in latter section.

In the tracer application segment (~25 cm), a flux (Neumann) boundary condition was used whose value was obtained as follows. The flow rate covered the width (60 cm) of the tank and 25 cm in the seaward direction. Because the model is two-dimensional (a vertical slice), the flux per unit width of tank (~5.0×10^{-5} m^2/s) was adopted, while the injection concentration of 2.76 g/L was assigned to the boundary as a Dirichlet boundary condition. Before and after the tracer application period, the no-flow and zero dispersion flux Neumann boundary condition were applied.

3.2.2 Modeling of Sea Level Fluctuation

The tide-induced seawater fluctuation can be expressed as follows:

$$h_{tide} = A\sin(\omega t), \tag{3.2}$$

where A denotes the amplitude of tides; ω denotes the frequency of the tides.

The wave-induced sea level fluctuation was simulated by using software FLUENT, a Computational Fluid Dynamics (CFD) modeling tool. The hydrodynamic model defined in FLUENT for the simulation is based on the Averaged Reynold Navier-Stokes equations, k-epsilon turbulence closure, and the Volume-Of-Fluid method. In the simulation, FLUENT required a very small time step (5×10^{-3} s) to simulate the sea level oscillation due

to waves. To simulate the groundwater flow and subsurface solute transport under these high-frequency sea level oscillations at the seaward boundary of the beach, a small time step (1×10^{-2} s) was also required in MARUN model. Therefore, the simulations resulted in an extremely high computational cost. For the sake of the feasibility of this high-frequency sea level oscillation modeling, a new approach, flow-averaged, was introduced in this study. Within this approach, several wave periods was first run in FLUENT to simulate wave-induced temporal pressure oscillations along the beach face. Then, the pressure oscillations were set as the seaward boundary condition in MARUN to simulate the net infiltration rate along the swash zone of the beach during a wave period. The estimated net flow rate was added to the swash zone of the beach as Neumann boundary condition in MARUN model to represent the effect of waves on the groundwater flow and solute transport; the time step used for the simulation can be increased to one wave period instead of subdivision of the period, which is numerically feasible for simulating the combined wave and tide forcing scenario. To validate this approach, both phase-resolved and flow-averaged approaches were adopted to simulate the Scenario 1 for comparison. The comparison results are shown in latter section.

3.3 Results and Discussion

3.3.1 Validation of Flow-averaged Approach

Figures 3.1a and 3.1b show the estimated wave run-up and run-down on the beach from FLUENT simulation. Blue and red colors denote air and water phases, respectively. The results show that the maximum run-up is ~5.5 cm above the SWL and the minimum run-down is ~2.5 cm above the SWL. Therefore, the length of the swash zone along the

beach is estimated to be 30 cm. The estimated wave run-up is consistent with the result calculated from early practical formulas (Hughes, 2004), shown as follows.

$$\frac{R}{H} = \frac{\tan\beta}{\sqrt{\frac{H}{L_0}}}, \tag{3.3}$$

where R is the maximum vertical run-up above SWL; H is wave height; L_0 is wave length; β is beach slope angle. The maximum run-up estimated from the eq. (3.3) is ~5.0 cm, which is consistent with our simulation results.

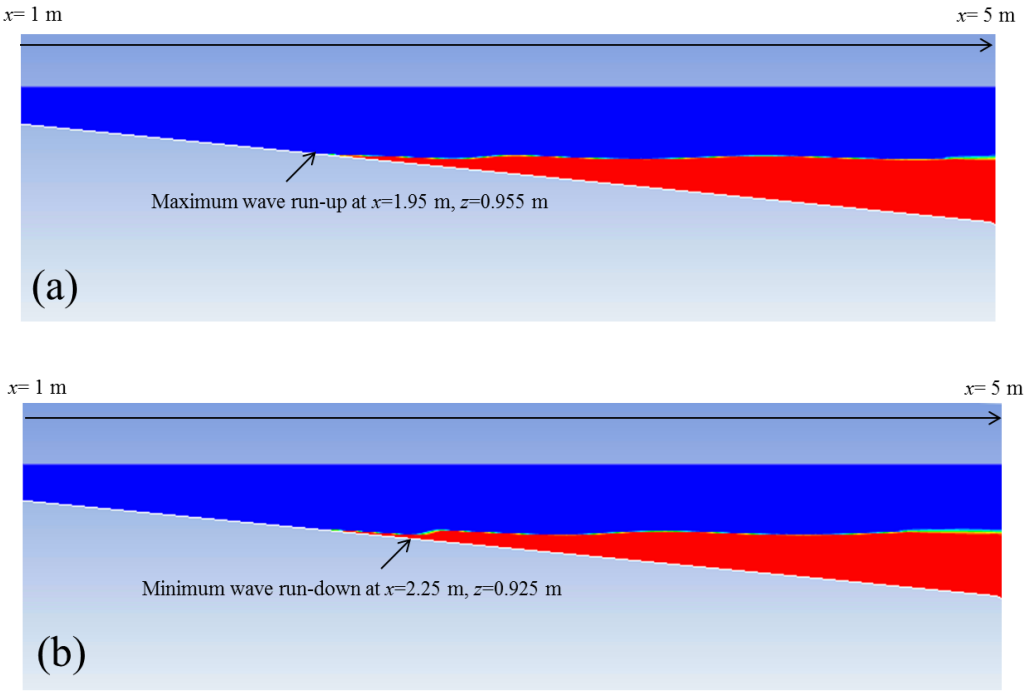

Figure 3.1 Simulated wave run-up (a) and run-down (b) on the beach in FLUENT.

Figure 3.2 shows the distribution of exfiltration and infiltration rates across the swash zone of the beach, which were averaged by several wave periods. The results suggest that large seawater infiltration occurred at the upper part of the swash zone, while

wave-induced groundwater exfiltration occurred at the lower part of the swash zone. The results also indicate an extensive mixing between seawater and groundwater in the swash zone of the beach. Wave-induced pressure gradients drove seawater to infiltrate to the beach from the upper part of the swash zone. The seawater infiltration mixed with groundwater and discharged into the ocean at farther seaward of the beach. The net flow rate across the swash zone was estimated to be -1.38 $m^3 day^{-1} m^{-1}$.

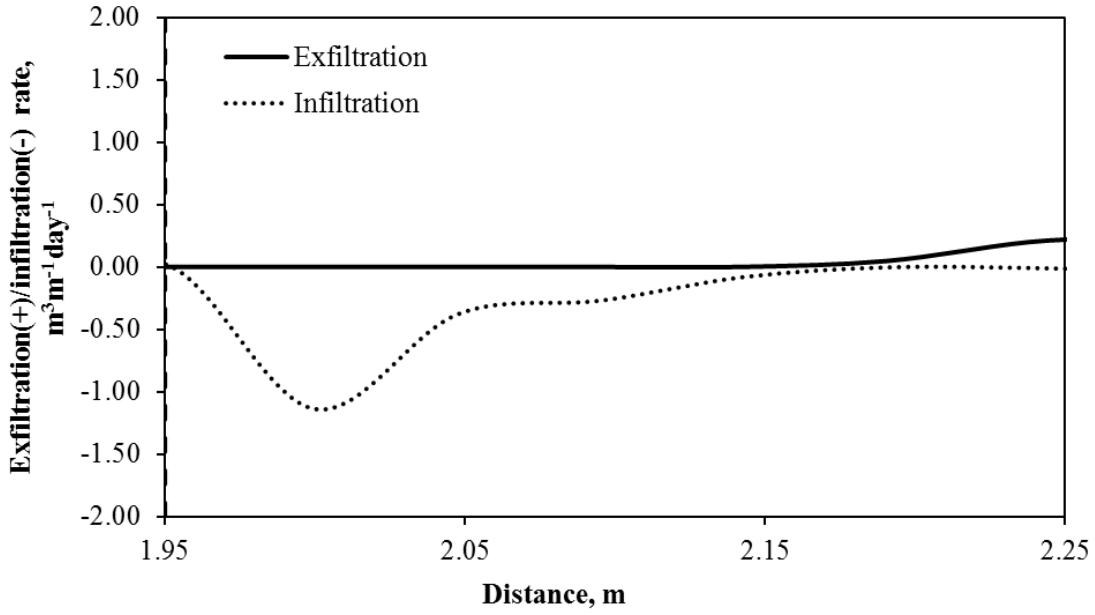

Figure 3.2 Distribution of groundwater exfiltration and seawater infiltration rates along the swash zone of the beach.

The flow-averaged approach adopted in this study was validated by comparing the simulation results of solute transport to direct phase-resolved approach and phase-averaged approach developed by Xin et al. (2010). Figure 3.3a shows the simulated trajectories of the plume centroid by different approaches. Among these methods, because of complete solving the phase in each extremely small time step, phase-resolved could reflect all the characteristics of waves acting onto the beach and present more accurate results for the

subsurface solute fates. While, similar results obtained from flow-averaged indicate the feasibility of using flow-averaged to represent the effects of waves on groundwater flow and solute transport in the beach. Compared to phase-resolved, both phase-averaged and flow-averaged seem to underestimate the farthest seaward location that the plume could reach beneath the beach. The plausible explanation for this underestimation is that flow-averaged approach averaged in/exfiltration rate across the swash zone and therefore diminished wave-induced pressure gradient along the swash and surf zone of the beach. However, in terms of the infeasibility of direct phase resolving due to the extremely high computation cost, the small difference of the results due to flow-average adoption would be acceptable. Figure 3.3b shows the variation of normalized mass of the plume as a function of time. The mass variations simulated by flow-averaged are similar to the results obtained by phase-resolved, which confirms that flow-averaged captured most characteristics of waves affecting solute transport beneath the beach surface.

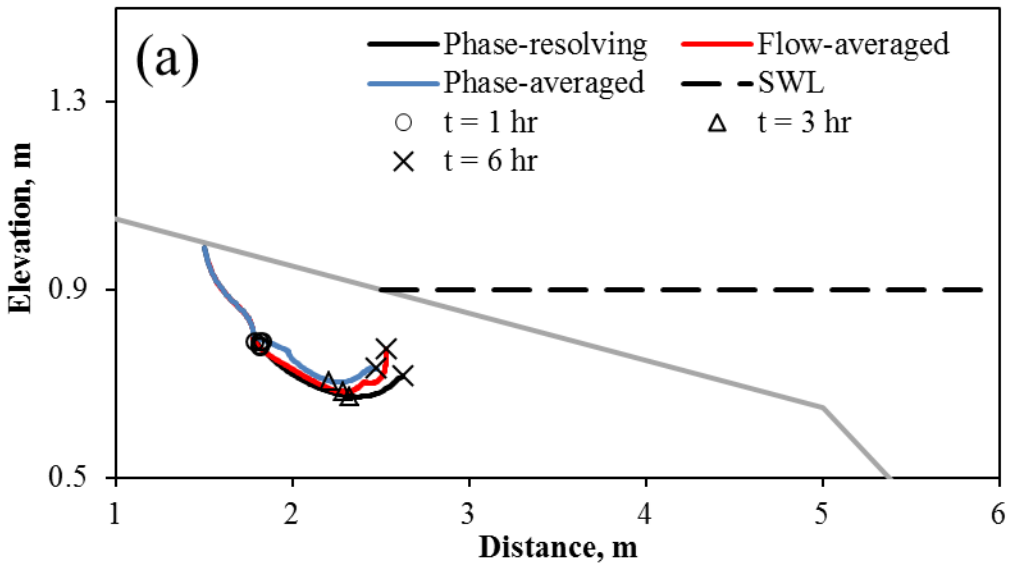

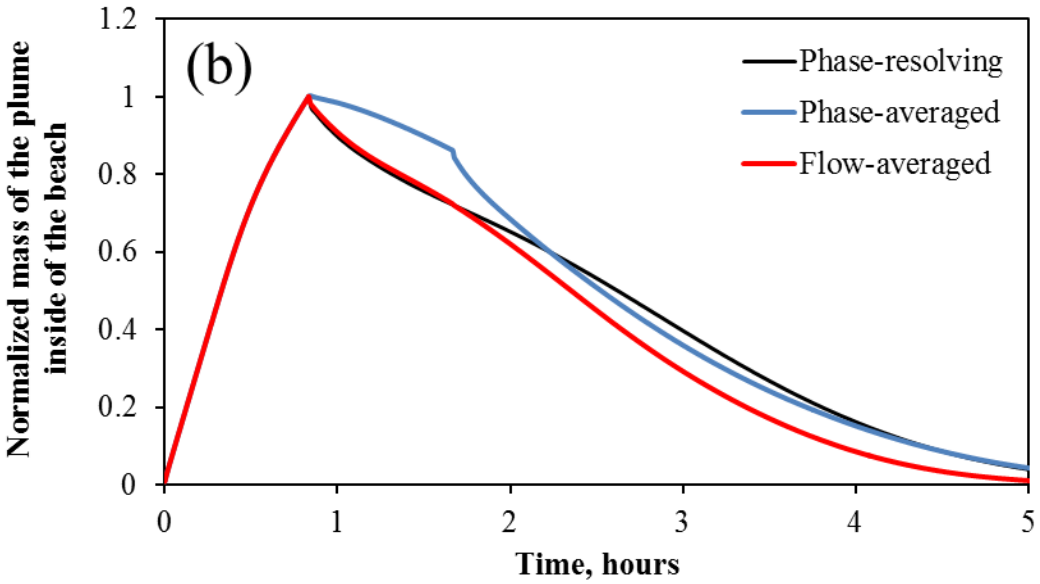

Figure 3.3 (a) Simulated trajectories of the plume centroid in the beach by using different approaches (phase-resolved, phase-average, and flow-averaged). The locations of the plume centroid at specific time are shown as symbols; (b) Variation of normalized mass of the plume as a function of time. The mass of the plume is normalized by its maximum value which occurred 50 min after injection.

3.3.2 Effects of Waves on Subsurface Solute Transport

Figure 3.4 shows the temporal variation of solute concentration contours along with groundwater table under the wave forcing, Scenario 1 (H = 4 cm, T_w = 1.11 s). Based on the simulation results, after the injection the plume migrated along the beach surface and discharged near the water table's exit point of the beach. Due to waves acting onto the beach, when the plume reached the swash zone, it started to migrate deeper and around an upper plume, which is formed by wave-induced seawater-groundwater circulations. It indicates that wave forcing affects the plume's pathway beneath the beach as the plume approaches the swash zone of the beach. This impact mainly depends on the extent of upper plume formed by high frequency wave forcing. Larger upper plume extent push the injected solute to migrate deeper and discharge further seaward.

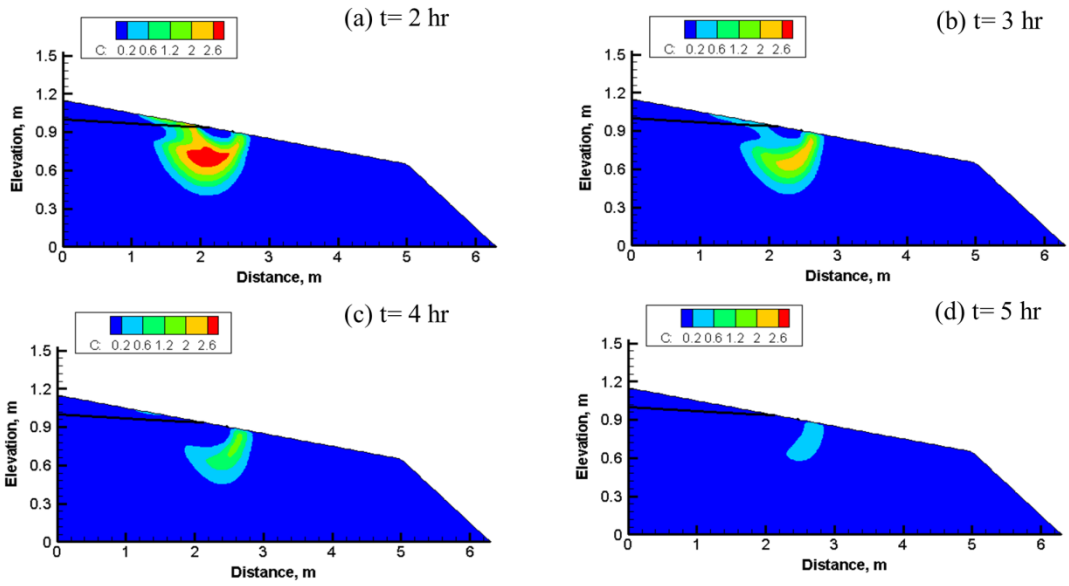

Figure 3.4 (a-d) Concentration (in g/L) contours at different time along with groundwater table (solid lines) for Scenario 1 (H = 4 cm, T_w = 1.11 s).

Figure 3.5a shows the simulated trajectories of the plume centroid beneath the beach under different wave conditions (Scenario 1 (H = 4 cm, T_w = 1.11 s), 2 (H = 4 cm, T_w = 2 s), and 3 (H = 8 cm, T_w = 1.11 s)). Compared to Scenario 1, the wave period and height were increased almost two times in Scenario 2 and 3, respectively. The results illustrate that under a more intensive wave forcing (a larger wave height or a longer wave period), the solute plume tended to migrate deeper into the beach and discharge farther seaward. This behavior is probably due to that a larger wave height or a longer wave period intensifies the groundwater-seawater circulation in the swash zone of the beach, and subsequently forms a larger upper mixing plume, which may push the injected solute further downwards as the solute approaches the swash zone. This impact also results in a longer pathway for solute to discharge into the ocean. Figure 3.5b shows the variation of the plume mass beneath the beach face. Note that the mass is normalized by its maximum value which occurred 50 min after the injection. The discharge of the plume tended to be

slower for the scenario under the condition of a larger wave height or a longer wave period. The results indicate that different wave properties also affect the plume's discharge rate and residence time. A larger wave height and/or a longer wave period decreased the plume's discharge rate and subsequently increase its residence time beneath the beach.

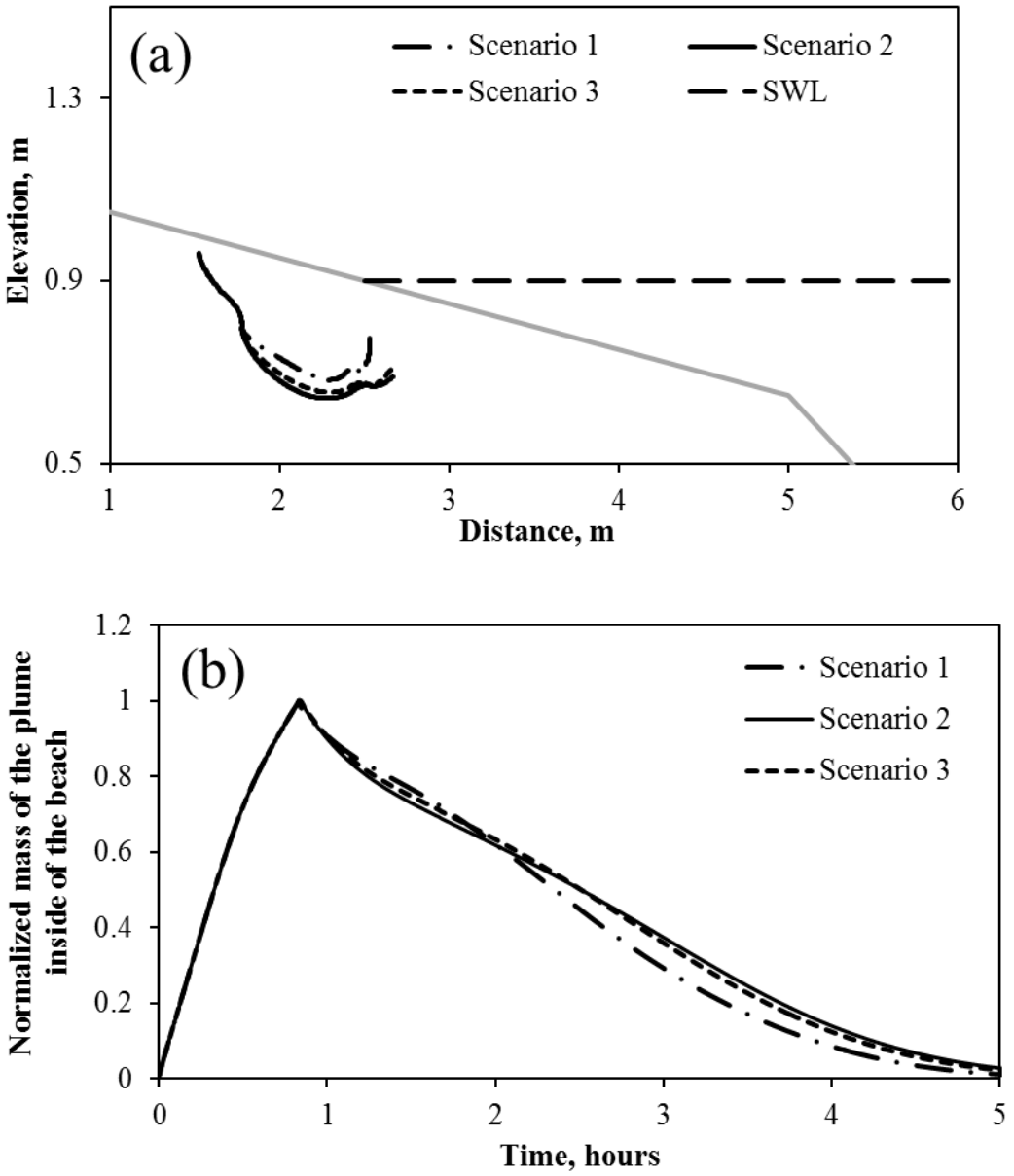

Figure 3.5 (a) Simulated trajectories of the plume centroid in the beach under different wave conditions (Scenario 1 (H = 4 cm, T_w = 1.11 s), 2 (H = 4 cm, T_w = 2 s), and 3 (H = 8 cm, T_w = 1.11 s)); (b) Variation of normalized mass of the plume as a function of time. The mass of the plume is normalized by its maximum value which occurred 50 min after injection.

3.3.3 Effects of Tides on Subsurface Solute Transport

Figure 3.6 shows the temporal variation of solute concentration contours along with groundwater table under the tide forcing, Scenario 4 (A = 0.4 m, T_t = 37.5 min). After the injection, the plume migrated along the beach face and discharged at the low tide zone of the beach. The results illustrate that the behavior of tides and waves affecting solute fates beneath the beach are apparently different. In Scenarios 1-3, under different wave forcing, the injected plumes totally discharged into the ocean within 6 hours; while, under the tide forcing (Scenario 4), the plume contour can still be observed at time t=10 h. Meanwhile, due to tides, the plume's discharge zone shifted further seaward (from water table's exit point to low tide mark). Therefore, compared to waves, tide forcing significantly elongated the plume trajectory beneath the beach and subsequently increased the plume's residence time, decreased its discharge rate, and shifted its discharge zone farther seaward.

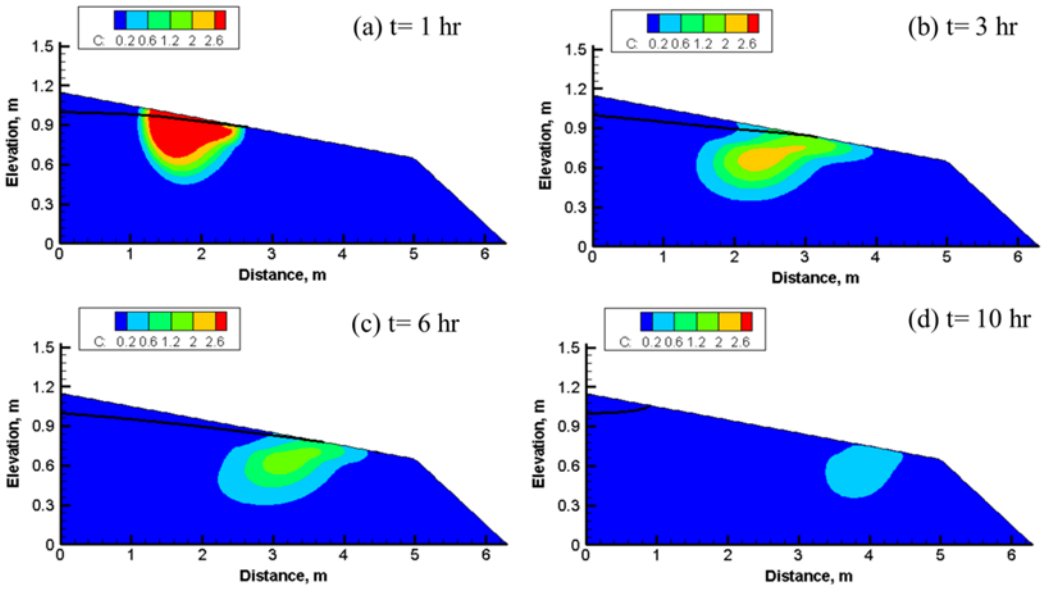

Figure 3.6 Concentration (in g/L) contours at different time along with groundwater table (solid lines) for Scenario 4 (A = 0.4 m, T_t = 37.5 min).

Figure 3.7a shows the simulated trajectories of the plume centroid in the beach under different conditions of tides (Scenario 4 (A = 0.4 m, T_t = 37.5 min), 5 (A = 0.3 cm, T_t = 37.5 min), and 6 (A = 0.4 m, T_w = 75 min)). Under different tide amplitude conditions (Scenario 4 and 5), the plume showed a different trajectory as it migrated beneath the beach. The injected solute tended to migrate farther seaward under a larger tide amplitude condition. The explanation for this behavior is that tides always drive the injected plume to migrate along the beach face and discharge at low tide zone of the beach; while, the low tide mark is lower when the beach is subjected to a larger amplitude tide. Therefore, under a larger amplitude tide condition, the plume can be driven farther seaward. The results also illustrate that, under different tide periods with the same amplitude (Scenario 4 and 6), the centroid of the injected plume shows almost the same trajectory, which indicates that the effect of tide period on solute transport is not significant compared to that of tide amplitude. Figure 3.7b shows the variation of the plume mass beneath the beach face. Note that the mass is normalized by its maximum value which occurred 50 min after the injection. The discharge of the plume tended to be faster for Scenario 5 under a smaller tide amplitude condition, while the discharge of the plume tended to be the same under two different tide periods (Scenario 5 and 6). The results indicate that tide properties also affect the plume's discharge rate and associated residence time. Larger tide amplitude induces a lower solute discharge rate and subsequently increases its residence time beneath the beach; while tide period has less impact on solute fates than tide amplitude.

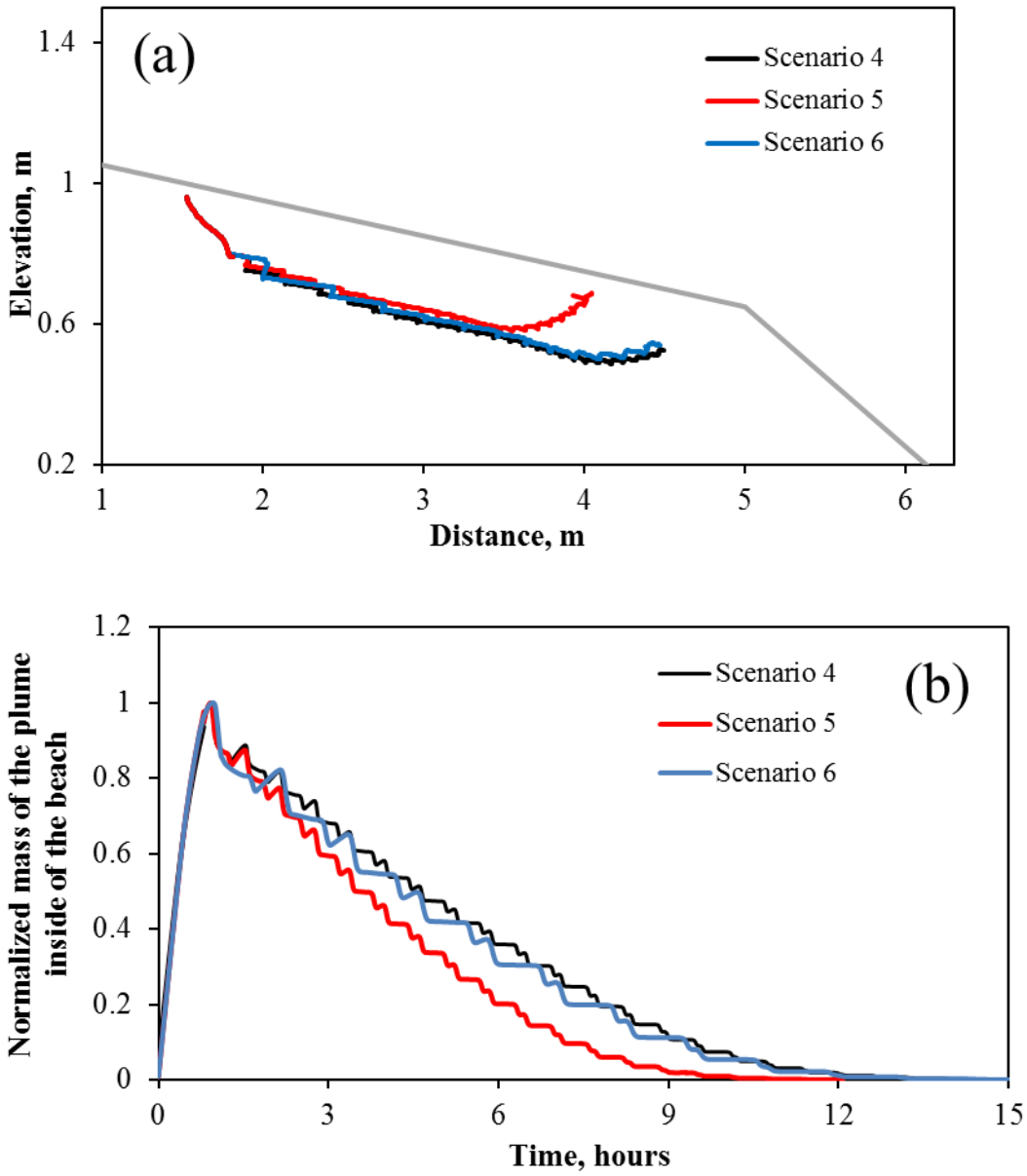

Figure 3.7 (a) Simulated trajectories of the plume centroid in the beach under different tide conditions (Scenario 4 (A = 0.4 m, T_t = 37.5 min), 5 (A = 0.3, T_t = 37.5 min), and 6 (A = 0.4 m, T_t = 75 min)); (b) Variation of normalized mass of the plume as a function of time. The mass of the plume is normalized by its maximum value which occurred 50 min after injection.

3.3.4 Effects of Combined Waves and Tides on Subsurface Solute Transport

Groundwater table, the velocity field, and degree of water saturation at four different times under the combined tide and wave forcing (Scenario 7) and the tide forcing (Scenario 4) were shown in Figure 3.8. The groundwater table fluctuated mainly with tidal induced sea-level oscillations. At high tide, large seawater infiltrated into the beach near the exit point of groundwater table. While, at falling mid-tide, rising mid-tide, and low tide, seawater infiltrated into the beach at landward of groundwater table's exit point and the infiltration mixed with groundwater discharged further seaward. These behaviors indicate an extensive seawater-groundwater exchange along the intertidal zone of the beach. Besides tide effects, waves affecting groundwater flow could be noticed by comparing the results between Scenario 4 and 7. Compared to separate tide forcing, under the combined forcing, water table's exit point shifted farther landward in all four different tidal phases. Meanwhile, the moisture content was also greater at the landward of the exit point, which is due to the wave-induced seawater infiltration in swash zone of the beach. The fact that wave-induced seawater infiltration enhances groundwater table in costal aquifers has been reported in previous studies (Kang et al., 1994; Boufadel et al., 2007).

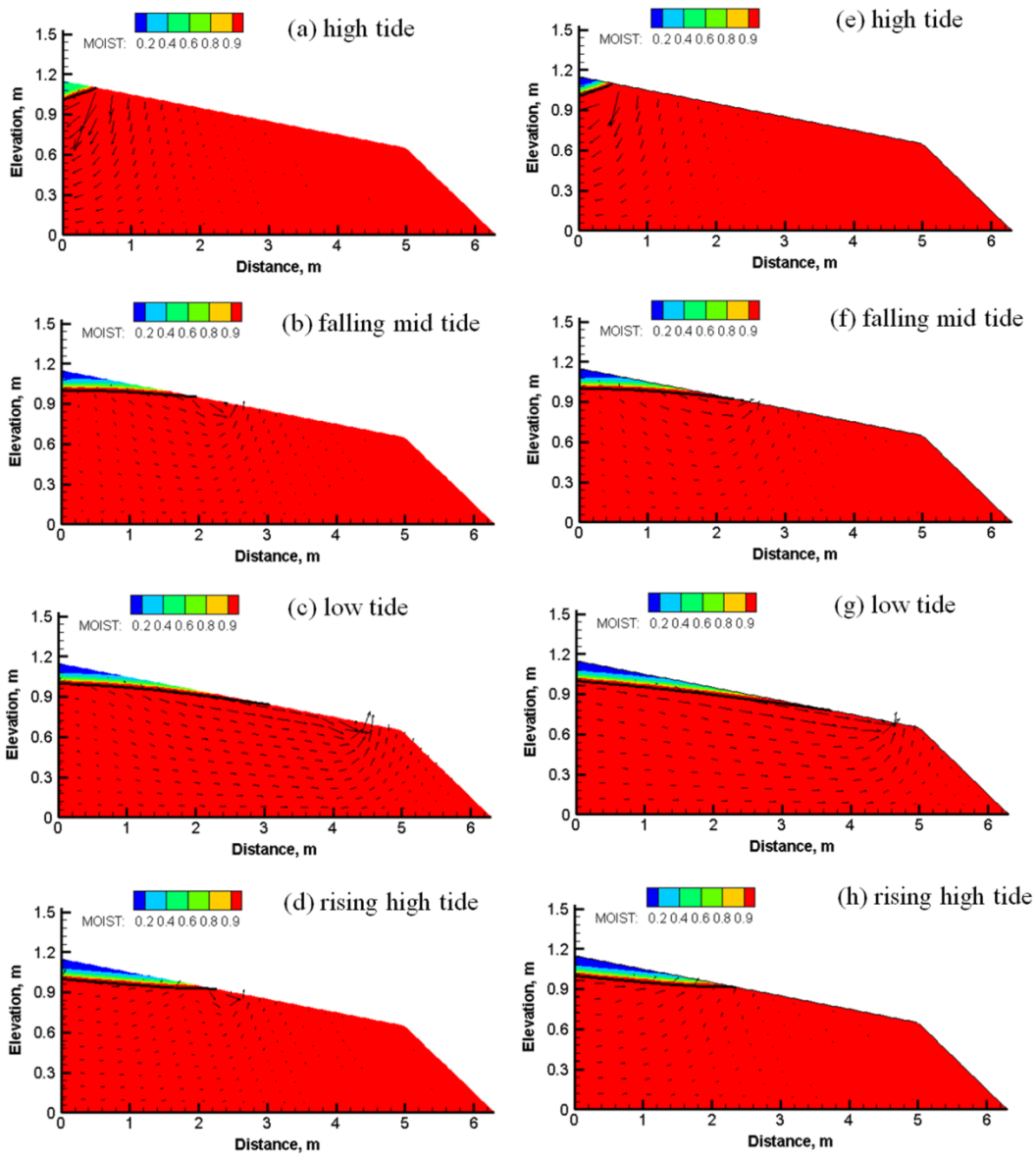

Figure 3.8 Groundwater table, the velocity field, and degree of water saturation at four different times under the combined forcing (a-d, Scenario 7 (A = 0.4 m, T_t = 37.5 min, H=4 cm, T_w=1.11 s)) and separate tide forcing (e-h, Scenario 4 (A = 0.4 m, T_t = 37.5 min)). The solid lines represent the beach water table. The arrows represent the Darcy flux. The contour denotes the degree of water saturation.

Figures 3.9a-3.9d shows the temporal variation of solute concentration contours along with groundwater table under the combined forcing condition (Scenario 7). The results illustrate that after the injection the plume migrated to seaward of the beach and

discharged at the low tide zone of the beach. During the migration, the mass of the plume tended to decrease, which could be detected by the shrink of the plume area during the migration. The decrease is most likely due to the dilution by the surrounding low salinity water and the discharge of the plume along the beach surface. The migration of the injected plume is similar to the results under separated tide forcing. However, the effect of waves on subsurface solute transport could still be noticed. Compared to separate tide forcing, due to the addition of wave forcing, the plume's tail and front were pushed further downward at time t = 3 hr and t = 6 hr, respectively. At time t = 10 hr, the area of plume was larger when combined oceanic forcing was acting onto the beach. These results indicate that wave-induced seawater-groundwater circulation impacts the injected solute's trajectory and residence time in the beach.

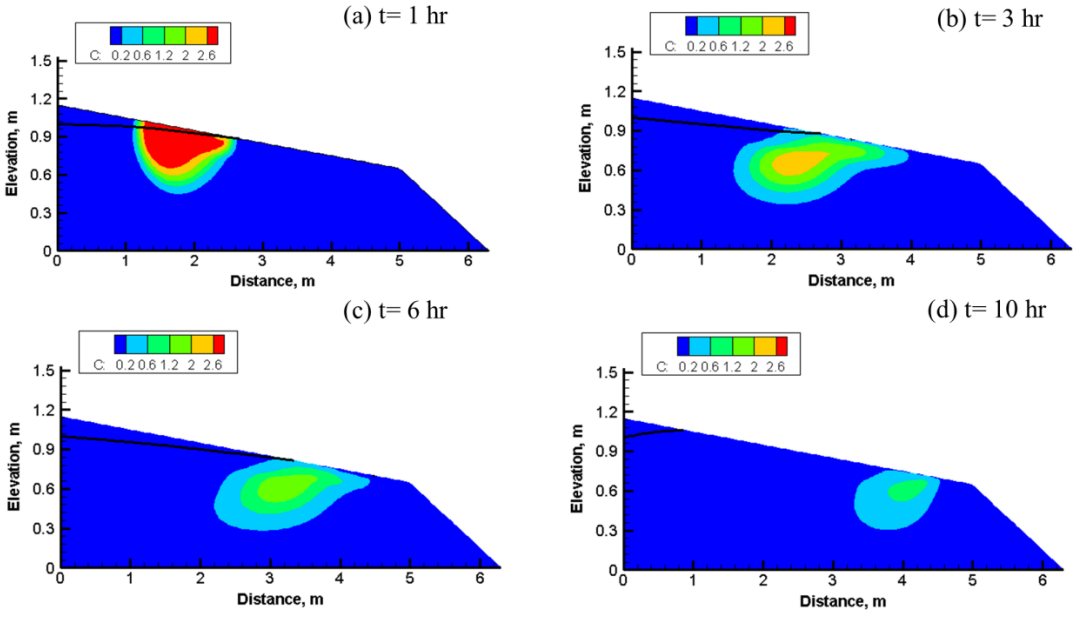

Figure 3.9 (a-d) Concentration (in g/L) contours at different time along with groundwater table (solid lines) under the combined tide and wave forcing.

Figure 3.10a shows the simulated trajectories of the plume centroid in the beach under different oceanic forcing (Scenarios 1, 4, and 7). Compared to the separate wave forcing (Scenario 1), the plume under tide-included oceanic forcing condition (Scenarios 4 and 7) seems to travel a longer pathway in the beach prior to discharge to the ocean. The trajectory length of the plume is 1.47 m, 3.66, and 3.64 m for Scenarios 1, 4, and 7, respectively. Therefore, tide forcing increased the plume's trajectory length two times in comparison to the scenario in absence of tides. Under tide forcing, the effect of additional waves on plume's trajectory length is negligible. However, waves, to some extent, modified the pathway of plume; the plume migrated further downward for both the Scenario 1 and 4. The average speed of the plume migration was calculated to be 0.21 m/h, 0.23 m/h, and 0.22 m/h for Scenarios 1, 4, and 7, respectively. Almost the same migration speed for different oceanic forcing indicates that the plume's trajectory and residence time would be more critical for one to investigate different oceanic forcing affecting the solute fates in coastal beaches.

Figure 3.10b shows the variation of the plume mass as a function of time for different oceanic forcing. The mass of the plume is normalized by its maximum value which occurred 50 min after the injection. The results indicate that different oceanic forcing significantly impacts the residence time of the plume beneath the beach. Under the separate wave forcing, the plume totally discharged to the ocean within 6 h; while, it approximately took 12 h for the plume to discharge to the ocean under tide-included oceanic forcing. Under tide forcing, additional waves decreased the discharge rate of solute in the beach. For instance, after 9 h, 10% of the total solute mass remained in the beach subjected to separate tide forcing, while 20% of the total solute remained when the

combined forcing was acting onto the beach. The plausible explanation for this behavior is that additional waves pushed the plume further downward, and the plume had to travel a longer pathway for discharge into the ocean. This behavior subsequently decreased the discharge rate of the plume.

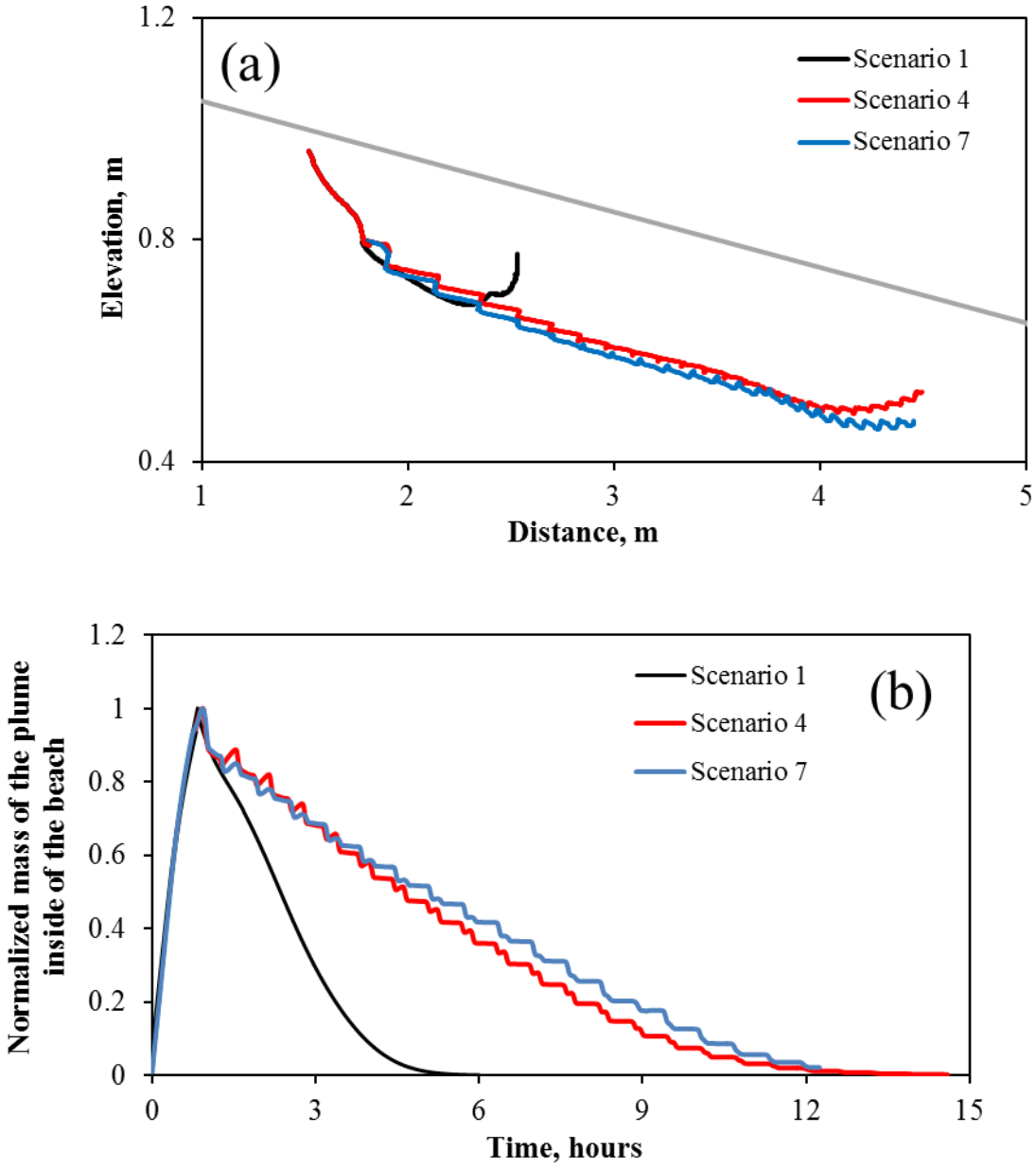

Figure 3.10 (a) Simulated trajectories of the plume centroid in the beach for different oceanic forcing. The locations of the plume centroid at specific time are shown as symbols; (b) Variation of normalized mass of the plume as a function of time for different oceanic forcing. The mass of the plume is normalized by its maximum value which occurred 50 min after injection.

3.4 Conclusion

Oceanic forcing is a critical factor affecting solute fate in coastal aquifers. A numerical study was conducted to investigate the fate of solute in coastal beaches subjected to high (waves) and low (tides) frequency oceanic forcing. A new approach, flow-averaged, was developed to generalize wave motions acting onto the beach for the sake of the feasibility of numerical computation. Simulation results suggested that different oceanic forcing significantly impacts the injected plume's trajectory, residence time, discharge zone and discharge rate. Waves caused the plume to migrate with a deeper trajectory in the beach and discharged at the groundwater table exit point of the beach; while, tides caused the plume to travel a longer pathway and discharged at the low tide zone of the beach. In contrast to wave forcing, tide forcing significantly increased the plume's residence time beneath the beach, which caused a lower discharge rate across the beach face. The combined wave and tide forcing seemed to have all the characteristics of separate oceanic forcing affecting subsurface solute fates in coastal aquifers. Under the combined forcing, due to waves, the plume migrated deeper, and the shape of plume was modified by seawater-groundwater circulations in the swash zone; due to tides, the trajectory length of the plume significantly increased and the plume discharged farther seaward at the low tide zone of the beach. Therefore, both tide and wave forcing need to be account for when one wants to investigate subsurface solute transport in coastal beaches subjected to this combined oceanic forcing.

CHAPTER 4

A NUMERICAL MODEL FOR SIMULATING TRANSIENT EVAPORATION FROM BARE SALINE SOIL

4.1 General

In coastal zones, intense evaporation of water could give rise to the pore water salinity at the shallow layer of soil. This chapter is to investigate the effect of evaporation on subsurface salinity distribution in coastal zones. The beach selected for the investigation is located in Fort Pickens, Florida (30°19'N, 87°11'W). The study site is a bare sandy beach with a shallow groundwater table, which is approximately 1 m deep. Two transects were installed perpendicular to the shoreline within the supratidal zone of the beach. One transect consisted of four galvanized steel piezometer wells to measure the water level, while the other transect consisted of four stainless steel multiport sampling wells that were used to collect water samples at various depths below the beach surface. The salinity of the water samples was analyzed by Digital refractometer (300035, SPER SCIENTIFIC). In order to simulate transient evaporation from bare saline soils, a bulk aerodynamic formulation model was developed as a module added to the transport model MARUN, which is a 2-D finite element model for variably saturated, variably density water flow and solute transport in tidally influenced beaches. Numerous simulations were conducted to predict the evaporation-induced salinization in the saline soil with shallow water table under different soil properties.

4.2 Experiments in a Beach of Gulf of Mexico

The beach is located in Fort Pickens National Monument, Florida (Figures 4.1a and 4.1b), which is about 210 km north-northeast of the site of Deepwater Horizon oil spill in Gulf of Mexico. The beach was contaminated by the oil spill. The oil was deposited beneath ~0.15 m of clean sand as the form of residual oil by wave action during storm events. The oil-contaminated sediments layer was approximately 0.30 m deep. The studied beach was impacted by dual tide and the maximum tidal range was around 1 m.

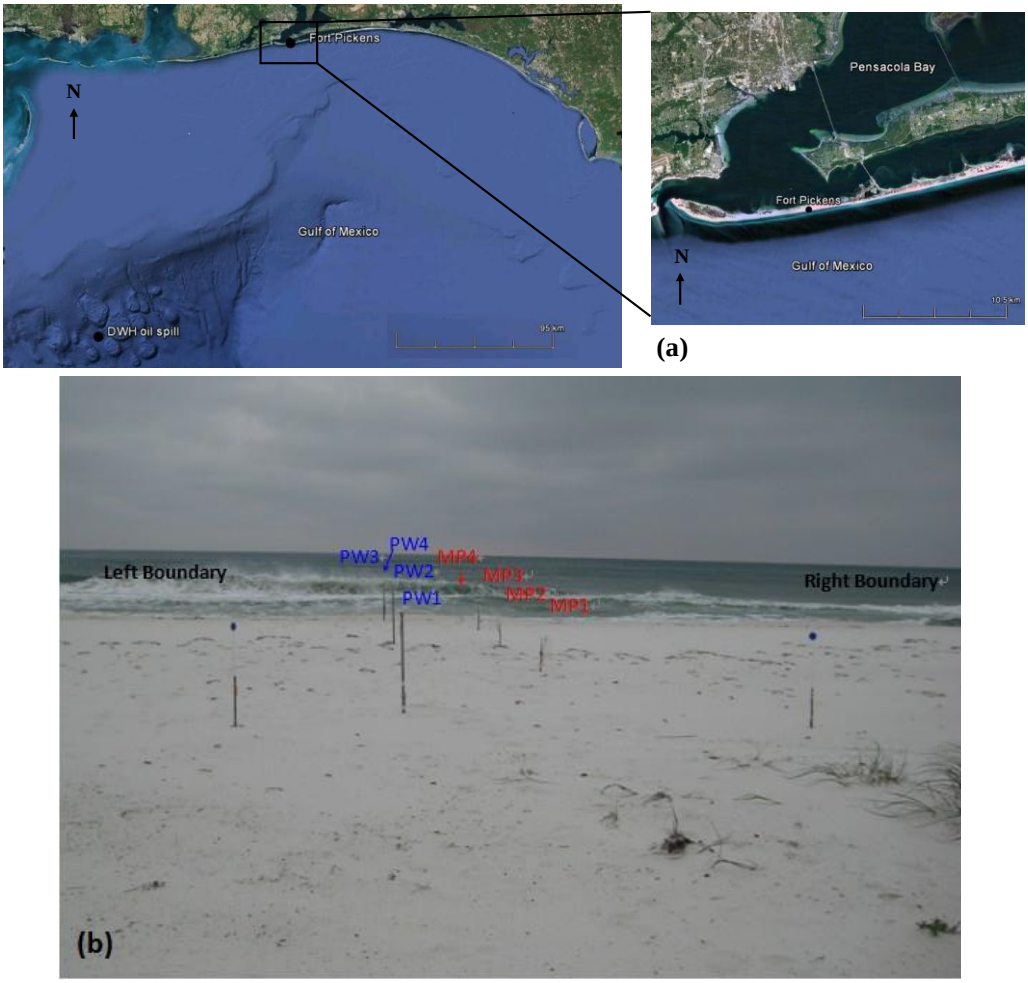

Figure 4.1 (a) Location of the studied beach on Fort Pickens, Florida (30°19'N, 87°11'W); (b) Site picture. Four piezometer wells (PW) and four multiport wells (MP) are shown.

Two transects were installed perpendicular to the shoreline within the region of the supratidal zone of the beach (Figure 4.1b). The distance between two transects is 2 m. One transect consisted of four stainless steel multiport sampling wells (MP) that were used to collect water samples at several discrete depths below the beach surface, and the other consisted of four galvanized steel piezometer wells (PW) that were used to measure the groundwater level. Beach topography survey was done by using Electronic Total Station (SET330R3, SOKKIA CO. LTD, Japan). Both transects were almost flat for the first 16.75 m, and then extended seaward with an average beach slope of 10%. The length of transects were around 48 m (Figures 4.2a and 4.2b).

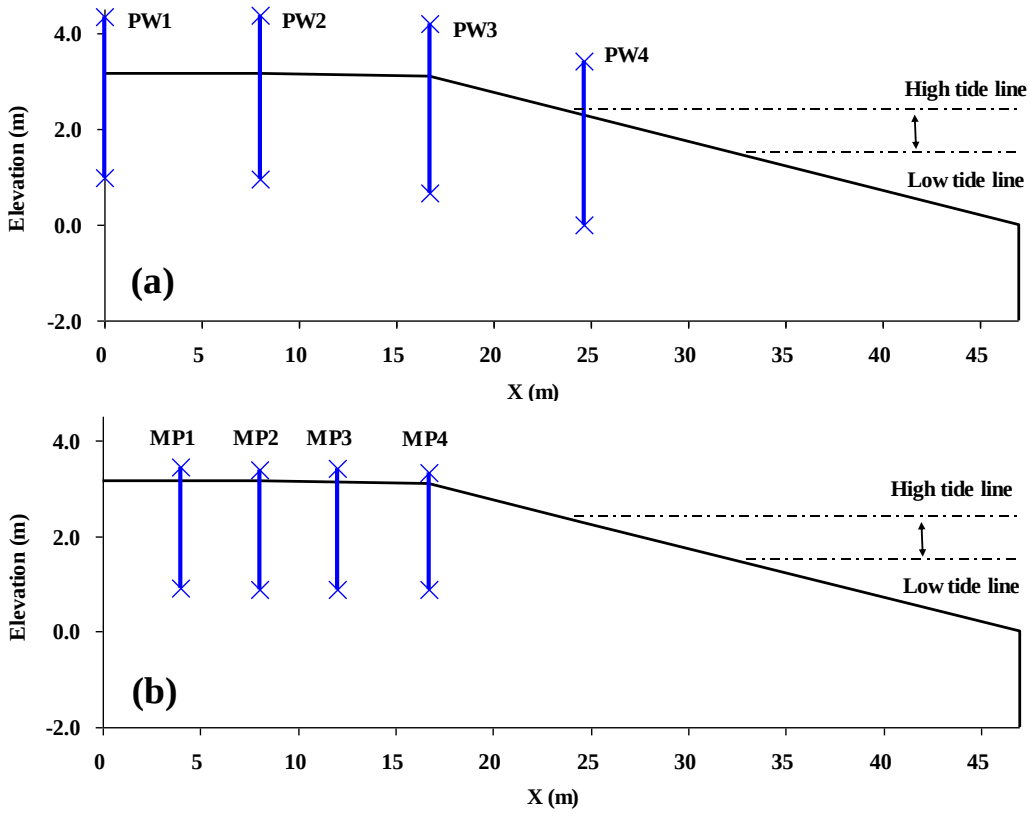

Figure 4.2 (a) Cross-sectional view of the transect which consisted of four piezometer wells; (b) Cross-sectional view of the transect which consisted of multiport wells.

For installation of wells along the transects, a hand auger was first used to drill holes and then the wells were set up in the holes. The range of eight installed wells depth below the beach surface was between 1.2 m to 2.3 m. The piezometer wells were made of 1-1/2 inch×36 inch galvanized drive point (J48-12-HomeDepot). It was extended to the surface using galvanized steel pipes and couplings. The drive points were perforated to allow water passing through them. The detailed information of well locations and sensor depths is reported in Table 4.1. A self-logging pressure transducer (Cera-Diver, Schlumberger) was placed at the bottom of each piezometer well to record the water pressure at every 10 minutes. A barometric (air) pressure sensor (BaroLogger, DL-500, Schlumberger) was used at the site and reported the barometric pressure at the same time and the same time interval. Water level was obtained by subtracting the barometric pressure from the readings of the pressure transducers in each piezometer well. The multiport sampling wells were made of stainless steel and contained ports at various levels. The ports were placed for each sampling well and were labeled by A to D from bottom up. The detailed information of well locations and port depths is listed in Table 4.1. Each port was connected via a tubing that extended to the top of the pipe. A tygon tube was placed on each of the tubing, which was connected to a luer lock three-way valve. To prevent blockage by fine sediments to guarantee good hydraulic connection between the beach pore water and the water inside the well, the multiport wells were wrapped with fine stainless steel screen.

Table 4.1 Elevations of Beach Surface, Sensors, and Ports at Different Locations

Location	*x* (m)	Surface Elevation z (m)	Depth of Sensor (m)			
PW1	0.0	1.85	1.47			
PW2	7.56	1.90	2.27			
PW3	15.2	2.05	2.22			
PW4	23.12	1.49	1.49			
Location	*x* (m)	Surface Elevation *z* (m)	Depth of Port A (m)	Depth of Port B (m)	Depth of Port C (m)	Depth of Port D (m)
MP1	3.48	1.85	1.58	1.12	0.89	0.66
MP2	7.32	1.90	1.43	1.13	0.83	0.53
MP3	11.16	1.93	1.46	1.16	0.86	0.71
MP4	15.20	2.04	1.22	1.07	0.77	0.47

Each pore water sample (approximately 100 ml) was collected by 60 ml Luer lock syringes and placed in 120 mL polyethylene bottles. They were shipped to the laboratory at Temple University in Philadelphia, PA, for chemical analysis of the salinity. The salinity was measured using digital refractometer (300035, SPER SCIENTIFIC) for each of the samples.

4.3 Bulk Aerodynamic Model

In order to quantify the complex water flux exchange between the soil surface and the atmosphere, the classic bulk aerodynamic method was adopted, and the evaporation flux can be expressed as follows (Mahfouf and Noilhan, 1991):

$$E_g = \frac{\rho_a}{R_a}(q_g - q_a), \tag{4.1}$$

where ρ_a is the air density [ML^{-3}], q_a is the air specific humidity [-], and R_a is the aerodynamic resistance [TL^{-1}], which is expressed by Liu et al. (2006) as follows,

$$R_a = 94.909 U_z^{-0.9036}, \tag{4.2}$$

where U_z is wind speed [LT^{-1}] at the atmospheric reference level (~2 m above the soil surface), and the surface specific humidity q_g can be expressed as (Lee and Pielke, 1992),

$$q_g = \alpha_1 q_{sat}(T_s), \tag{4.3}$$

where $q_{sat}(T_s)$ is the saturated specific humidity [-] at the surface temperature, T_s [Θ], defined as the solution of the surface energy balance, which can be expressed as follows (Singh, 2002),

$$q_{sat}(T_s) = \frac{0.622 e_{sat}(T_s)}{[P_0 - 0.376 e_{sat}(T_s)]}, \tag{4.4}$$

where P_0 is ground surface pressure [$ML^{-1}T^{-2}$], $e_{sat}(T_s)$ is the saturated vapor pressure [$ML^{-1}T^{-2}$] at temperature T_s [$ML^{-1}T^{-2}$]. The function of $e_{sat}(T_s)$ can be expressed as (Tetens, 1930),

$$e_{sat}(T_s) = 0.6108 e^{\frac{17.27 T_s}{T_s + 237.3}}, \quad (4.5)$$

The relative humidity of air at the land surface, α_1, has been parameterized as a function of the surface water content, w_g [-], expressed as (Barton, 1979; Lee and Pielke, 1992):

$$\alpha_1 = \min(1, \frac{1.8 w_g}{w_g + 0.30}), \quad (4.6)$$

4.4 Numerical Implementations

4.4.1 Model Setup

The simulated domain is 2 m × 2 m shown in Figure 4.3. Two scenarios were tested to investigate the effect of transient evaporation on groundwater flow and subsurface solute distribution in the domain without water supply (Scenario 1) and with surrounding water supply (Scenario 2). Simulations were also conducted to reveal the impacts of soil properties, such as permeability and capillarity, on the interaction between soil surface evaporation and the groundwater dynamics beneath the evaporation zone.

4.4.2 Initial and Boundary Conditions

The initial salinity was set at 25 g/L in the domain. The domain was assumed to be initially fully saturated for both scenarios. Evaporation zone was implemented on the top boundary of the domain between x = 0.5 m and x = 1.5 m. Neumann boundary condition, shown in equation (4.1), was assigned to the zone to describe evaporation flux between the soil

surface and the atmosphere, while Cauchy boundary condition was adopted to simulate salt accumulation below the soil surface due to evaporation. Zero flow and zero mass transport were adopted as boundary conditions were assigned at the rest of the segment on the top of the domain (shown in Figure 4.3). The Cauchy boundary condition is expressed as:

$$(\mathbf{q}c - \beta\phi SD \cdot \nabla c) \cdot \vec{n} = 0, \tag{4.7}$$

where $\vec{n}$ is the vector normal to the boundary. For Scenario 1, zero-flow and zero-mass transport were adopted as boundary conditions at the left and right sides of the domain. For Scenario 2, a Dirichlet boundary condition (a constant shallow water table) was assigned to these domain boundaries. It is given as:

$$\psi(x, z) = H_b - z(1 + \varepsilon c_b), \tag{4.8}$$

where H_b is equal to 1.8 m (0.2 m below the soil surface), c_b is equal to the initial salt concentration in the domain (25 g/L), and ε is fitting parameter for the density concentration curve.

The total simulation time was 20 hours. In order to select optimal time step for each simulation, numerical trials were conducted until further decrease of time step did not improve the accuracy of the solutions. The time step was 1 seconds.

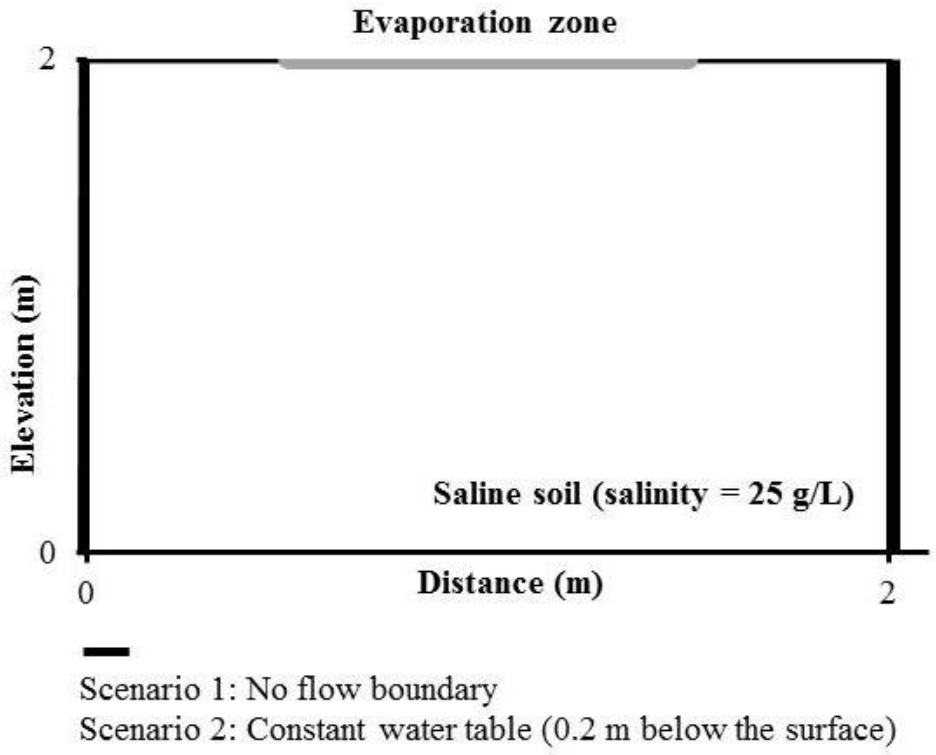

Figure 4.3 Schematic of the simulated domain along with the boundary types used for two scenarios. The evaporation zone (segment) is between x = 0.5 m and x = 1.5 m.

4.4.3 Model parameters

The summary of the parameter values used for the simulation is shown in Table 4.2. In order to obtain reasonable model parameters, soil properties were obtained from a beach located in Fort Pickens National Monument, Florida (30°19'N, 87°11'W). Sediment samples were collected from four different locations with three different depths. Sieve analyses were performed to determine the grain size distribution in sediment. The saturated hydraulic conductivity was estimated based on the grain size analysis using the Kozeny-Carman equation:

$$K_o = \frac{g}{\nu} \times 8.3 \times 10^{-3} [\frac{\phi^3}{(1-\phi)^2}] d_{10}{}^2, \quad (4.9)$$

where g is acceleration due to gravity [LT^{-2}], ν is kinematic viscosity of freshwater [L^2T], d_{10} represents the grain size at which 10% of the sample mass passed. The average value of the hydraulic conductivity was 1.0×10^{-3} m/s. The grain size distribution and hydraulic conductivity of all the sediment samples are reported in Table 4.3.

Table 4.2 Model Parameter Values Used in the Numerical Simulation

Symbol	Definition	Units	Value
α	Sand capillary fringe parameter of the van Genuchten [1980] model	$1m^{-1}$	4.75
n	Sand grain size distribution parameter of the van Genuchten [1980] model	-	8.5
K_o	Saturated freshwater hydraulic conductivity	ms^{-1}	0.9×10^{-4}
α_L	Longitudinal dispersivity	m	0.1
α_T	Transverse dispersivity	m	0.01
ε	Fitting parameter of density concentration relationship	lg^{-1}	7.44×10^{-4}
S_0	Specific storage	$1\ m^{-1}$	10^{-5}
S_r	Residual soil saturation	-	0.07
Φ	Porosity	-	0.41
CONVP	The convergence criterion of pressure head in the Picard iterative scheme of MARUN code	m	10^{-5}
τD_m	Product of tortuosity and diffusion coefficient	m^2s^{-1}	10^{-9}
T_s	Temperature	^oC	20
P_0	Atmospheric pressure at ground surface????	kPa	101.325
U_Z	Wind speed at the atmospheric reference level (~2.0 m above the soil surface)	ms^{-1}	1.0
ρ_a	Air density	kgm^{-3}	1.1839
q_a	Air relative humidity	-	0.2

Table 4.3 Grain Size Distribution, Porosity, and Estimated Hydraulic Conductivity.

Size of sieve opening (mm)	Percentage Passing (%)													
	PW1 55cm	PW1 85cm	PW1 140cm	PW1-2 55cm	PW1-2 85cm	PW1-2 140cm	PW2-3 55cm	PW2-3 85cm	PW2-3 140cm	PW3-4 55cm	PW3-4 85cm	PW3-4 140cm	Average	SD
2	100	100	99.81	100	100	100	99.90	99.80	100	100	100	96.08	99.63	1.07
0.841	99.33	99.71	98.16	99.07	100	99.82	98.91	99.80	100	100	100	95.76	99.21	1.17
0.595	90.39	91.81	91.06	93.61	99.25	97.70	91.91	96.06	96.90	95.34	97.27	94.96	94.49	2.78
0.42	56.89	60.15	61.47	63.28	80.06	71.29	56.98	74.21	69.64	71.20	78.44	83.77	68.95	8.78
0.297	13.70	13.09	13.73	15.38	20.84	14.13	12.00	18.44	12.97	13.98	28.55	33.17	17.50	6.50
0.177	2.70	0.81	0.92	1.43	0.30	0.18	0.67	1.28	0.28	0.09	0.23	0.72	0.80	0.70
0.149	1.98	0.52	0.18	0.81	0.15	0.09	0.41	0.99	0.28	0.09	0.15	0.08	0.48	0.53
0.074	0.67	0.12	0.09	0.25	0.15	0	0.10	0.30	0	0	0	0	0.14	0.19
Pan	0	0	0	0	0	0	0	0	0	0	0	0	0	0
Porosity (m^3/m^3)	0.41	0.42	0.41	0.4	0.43	0.41	0.395	0.38	0.413	0.39	0.45	0.43	0.412	0.018
K (m/s)	0.001	0.0012	0.0011	0.00086	0.001	0.0011	0.001	0.00062	0.0012	0.00085	0.0011	0.00084	0.0009	0.0001

Note: The hydraulic conductivity (K) is estimated by the Kozeny-Carman equation. In the last column, the arithmetic average of the Percentage Passing of the 12 samples is listed for different sieve openings. The average *K* is not the arithmetic average of *K*-values of the 12 samples, but is calculated also by the Kozeny-Carman equation using the data of the average percentage passing and average porosity in the last column.

Capillary retention experiments were conducted using collected sediment samples. A weighted least square objective function was used to estimate the values of capillary parameters as done in Boufadel et al. (1998b):

$$F = \sum_{i=1}^{N_K} \frac{(S_{a,i} - S_{o,i})^2}{S_{o,i}^{\ 2}}, \tag{4.10}$$

where $S_{a,i}$ is the analytical solution of the soil moisture ratio; $S_{o,i}$ is observed data from capillary retention experiment; N_K is the number of observed data. The nonlinear optimization model GRG2 was used to fit the van Genuchten model to the experiment data. Generalized Reduced Gradient (GRG2) Algorithm has been used in many environmental science works (Unver and Mays, 1984; Boufadel et al., 1998a; Geng et al., 2013). The capillary parameter values and their standard deviations are reported in Table 4.4.

Table 4.4 Descriptive Statistics for van Genuchten (1976) Water Retention Parameters

Capillary Parameters	Descriptive Statistics for these parameters			
	$\bar{x}$	s	CV	NS
α	4.75	0.49	0.10	12
n	8.49	0.69	0.08	12
S_r	0.02	0.0059	0.28	12

Here, $\bar{x}$, mean; s, standard deviation; CV, coefficient of variation = the ratio of the standard deviation to the mean; and NS, sample size.

4.4.4 Mesh Selection

The importance of the spatial discretization on the accuracy of simulating a strongly coupled groundwater-brine flow system has been proven in previous studies (Oldenburg and Pruess, 1995; Boufadel et al., 1999b). Therefore, in this study, numerical trials were

tested to explore a mesh resolution that would provide accurate solutions for the desired application within a feasible computation cost. Three meshes were adopted to discretize the domain: a coarse mesh (6561 nodes, $N_x \times N_z$ =81 × 81) grid resolution 2.5 cm, medium mesh (10201 nodes, $N_x \times N_z$ = 101 × 101) grid resolution 2.0 cm, and fine mesh (17956 nodes, $N_x \times N_z$ = 134 × 134) grid resolution 1.5 cm. For the sake of brevity, only Scenario 1 simulation results are presented in here. Figure 4.4 shows the simulated subsurface salinity contours at time t = 20 h using a coarse mesh (dashed lines), medium mesh (solid lines), and fine mesh (dash-dot lines). The salinity distributions are almost the same for the medium and fine meshes, suggesting that the medium mesh could provide accurate solutions and a finer mesh does not improve the results greatly. Therefore, the medium mesh was selected for latter simulations. To test the model accuracy, the total mass of salt in the domain was calculated at each time step. The difference for both scenarios was less than 4% during the simulation period, demonstrating the capability of model to conserve the mass balance.

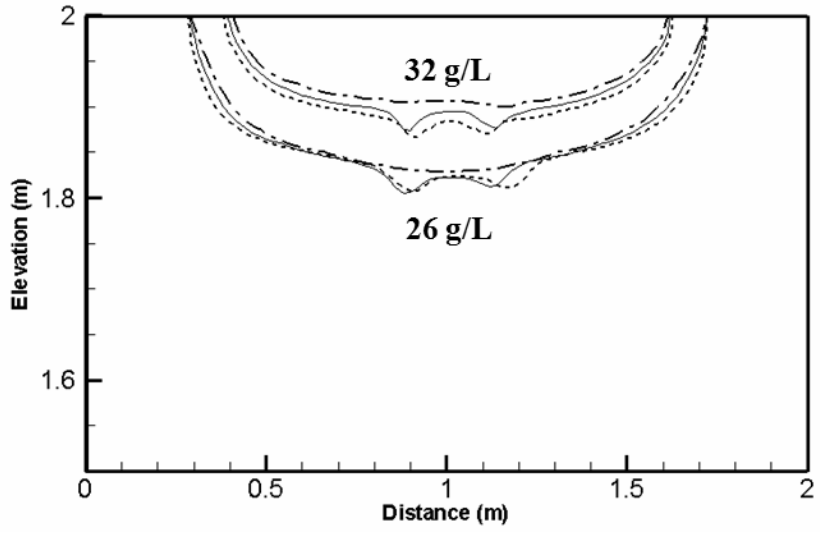

Figure 4.4 Simulated subsurface salinity contours at time t = 20 h using coarse mesh (dashed lines; mesh resolution: 2.5 cm), medium mesh (solid lines; mesh resolution: 2.0 cm), and the fine mesh (dash-dot lines; mesh resolution: 1.5 cm) for Scenario 1.

4.5 Results and Discussion

4.5.1 Salinity Distribution in the Field

Figure 4.5 shows the salinity distribution in the shallow layer of supretidal zone of the beach along with measured soil moisture content by using moisture meter. The salinity in this zone is much higher than that of seawater (35 mg/L). The reason is probably due to high evaporation occurring in this beach. The higher moisture content near the surface layer of the beach indicates that high evaporation rate extracts the water from the surface soil, while the total salt contained in the water still stays in the residual pore water of the beach, which induces the salinity higher than that of seawater.

Depth (m)	Moisture	Salinity (g/L)
0.05	20%	191
0.15	60%	165
0.35	80%	143
0.5	80%	19

D	M	S
0.05	40%	SL
0.15	80%	94
0.35	70%	187
0.5	70%	162

D	M	S
0.05	50%	SL
0.15	60%	125
0.35	80%	212
0.5	100%	173

D	M	S
0.05	20%	351
0.15	90%	134
0.35	90%	215
0.5	100%	77

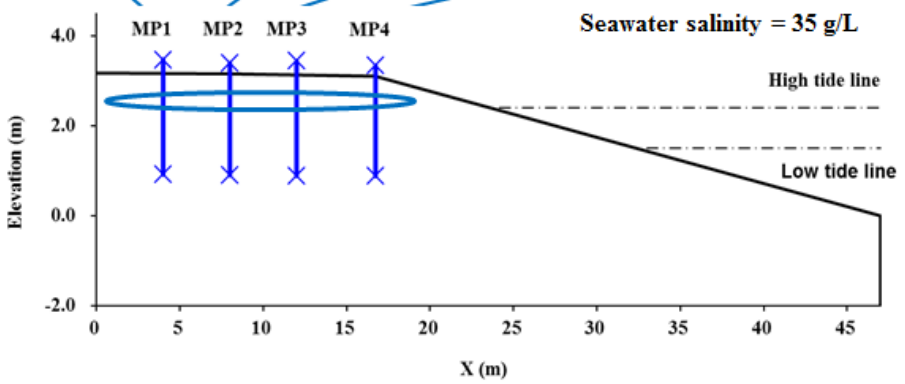

Figure 4.5 The pore water salinity distribution in unsaturated zone of the beach.

Figure 4.6 shows the pore water salinity distribution in the saturated zone of the beach. It shows a classic wedge shape of salinity distribution at the saturated part of the beach. The lower salinity of landward and higher salinity of seaward shows a gradually

decreasing density gradient along the seaward side in the transition zone of seawater wedge. The measurements is consistent with previous studies (Boufadel, 2000; Narayan et al., 2007; Li et al., 2008).

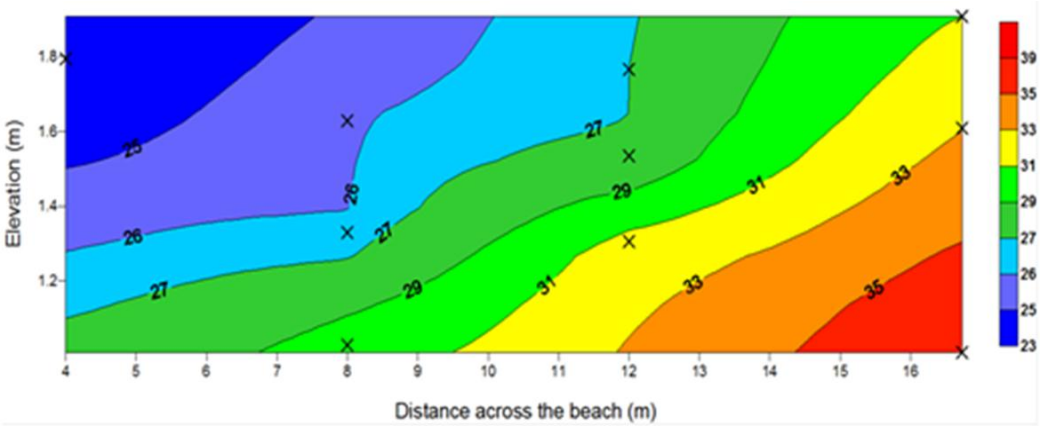

Figure 4.6 Spatial distribution of pore water salinity in saturated zone of the beach.

4.5.2 Simulation Results

4.5.2.1 Evaporation Rate. Figure 4.7 shows the simulated evaporation rate at soil surface as a function of time for the two scenarios. The evaporation rate for both scenarios dramatically decreased at first (a few hours for Scenario 1 and a few minutes for Scenario 2). Then, the evaporation rate of Scenario 1 decreased gradually with time, while it remained essentially constant in Scenario 2. Thus, the results indicate a different response when the two groundwater systems were subjected to the evaporation. Without the surrounding water supply (Scenario 1), the surface moisture at the evaporation zone decreased, approaching that in the atmosphere; this behavior led to the decrease of the evaporation rate at the soil surface. In Scenario 2, since the water table at the boundaries was constant, rather than reaching equilibrium with the atmospheric condition, the surface water content at the evaporation zone decreased until its associated evaporation flux

dropped to an amount that surrounding water could supply; then, the evaporation rate tended to be stable. It is also shown that with surrounding water supply the evaporation could remain at a relatively high rate when comparing between two scenarios.

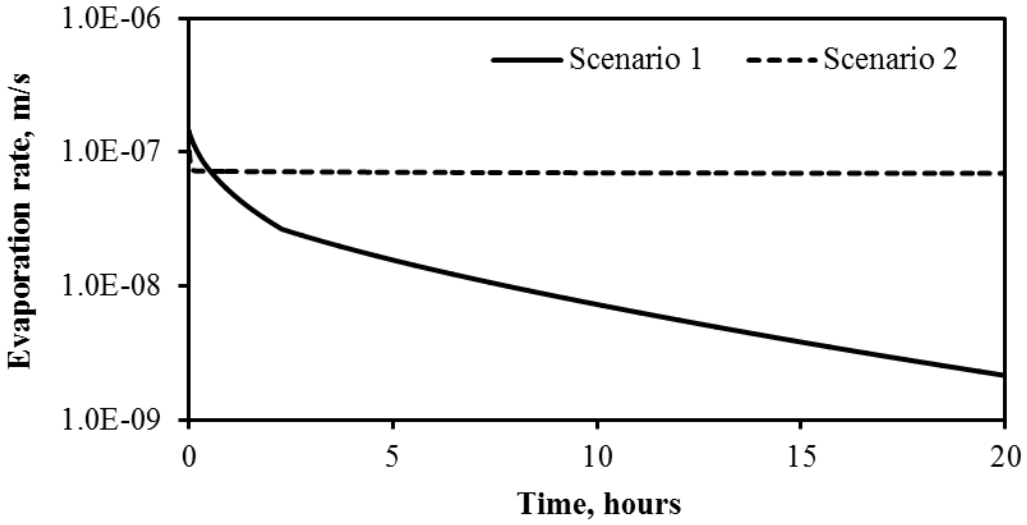

Figure 4.7 Evaporation rate at the soil surface for Scenario1 and Scenario2 as a function of time. Note the constant rate for Scenario 2.

4.5.2.2 Moisture Distribution. The simulated moisture distribution profiles for the two scenarios are shown in Figures 4.8a and 4.8b. Note that the soil moisture ratio is the horizontal average at each specific depth. In Scenario 1, the water content above the water table decreased approaching the equilibrium with the atmospheric condition (20% of saturated air specific humidity). In contrast, in Scenario 2, the surface moisture ratio dropped to 0.56, and then the subsurface moisture profiles tended to be stable. These results indicate the important role of surrounding water supply in determining the subsurface moisture distribution profile during the evaporation process. In absence of surrounding water supply (Scenario 1) the moisture distribution in the evaporation zone would depend on atmospheric conditions. During the evaporation, the soil moisture

decreased because water would be extracted from the soil surface. As the surface water content decreased to the level of atmospheric condition, the humidity gradient at soil-air surface tended to be zero and the amount of water evaporated from the soil would be negligible. At this stage, the subsurface moisture distribution profile would be stable. However, with the surrounding water supply (Scenario 2) to the evaporation zone, the soil surface water content could remain an amount higher than the atmospheric condition. The difference in water content between soil surface and atmosphere would induce a steady evaporation rate at the soil surface (shown in Figure 4.7).

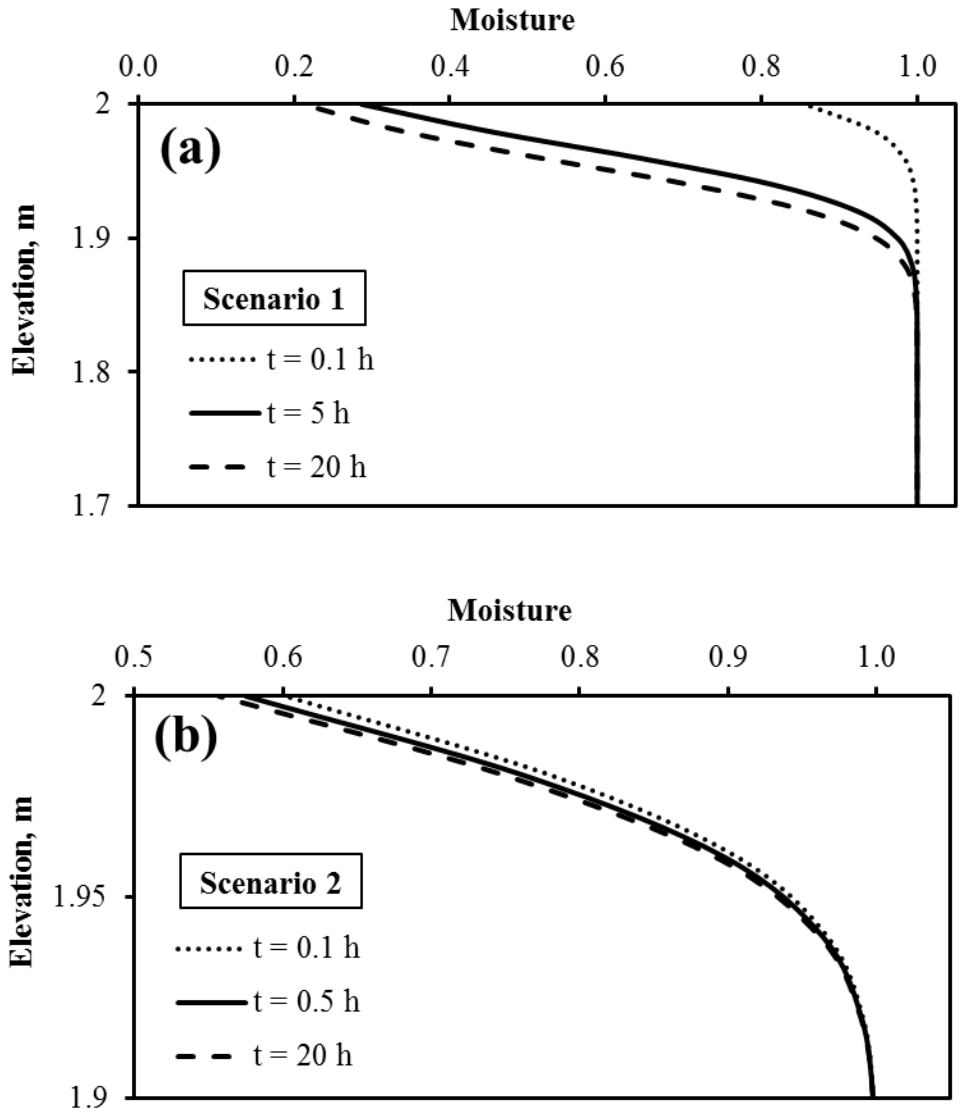

Figure 4.8 Moisture distribution profile below the surface (x=1 m) at different time for Scenario 1 (a) and Scenario 2 (b). The soil moisture ratio is the horizontal average at each specific depth.

4.5.2.3 Salinity Distribution. Figures 4.9a and 4.9b show the simulated salinity contours, velocity field, and groundwater table for Scenario 1 at time t = 5 h and 20 h. As the water was evaporated from the soil surface, the salinity at the shallow layer of soil increased, which formed a high salinity plume beneath the soil surface; meanwhile, due to the evaporation, the groundwater table dropped until significant upward flow was not

observed below the surface evaporation zone. At time t = 5 h, the high salinity plume spread evenly from the surface to the surrounding soil. In contrast, as the groundwater table tended to be stable at time t =20 h, the plume started to migrate downwards with a "finger" shape. The plausible explanation for this behavior is as follows: In the first few hours, the humidity gradient at soil-air interface drove pore water to evaporate from soil and subsequently formed a high salinity plume below the soil surface. Due to the evaporation from the soil surface, the groundwater flowed upwards, which was opposite to the direction of the plume migration (mainly in downward direction). Therefore, during this period, the plume migration to the surrounding soil was mostly as a result of molecular diffusion, which made the plume spread evenly. As the groundwater table dropped to the level at which the water content at soil surface nearly reached the equilibrium with atmosphere condition, the hydraulic exchange between the groundwater-brine system and atmosphere is negligible. Then, the spreading of the plume would be dominated by density-driven groundwater flow, which could be detected by the flow pattern near the bottom corners of the plume. Density difference at these edges induced groundwater flow circulation in their surrounding zone. These results are consistent with previous studies (Oldenburg and Pruess, 1995; Boufadel et al., 1999b; Frolkovič and De Schepper, 2000). They found that solute density difference would develop a circulation flow pattern and form a "finger" shape plume when dense brine was overlaid onto a groundwater system with fresh water. In contrast to previous studies, such as the Elder problem, the "finger" shape in this study is not quite distinct. The plausible reasons are as follows: (1) in the Elder problem, the density of dense brine and groundwater are 310 g/L and 0 g/L, while the salinity at soil surface and in groundwater are 70 g/L and 25 g/L. Therefore, less solute density difference would

result in less remarkable "finger" shape. (2) In the Elder problem, the groundwater system is fully saturated; in contrast, in this study, due to the evaporation, the "finger" shape plume appeared in unsaturated zone of the domain. Variable saturated condition might also impact the formation of the "finger" shape.

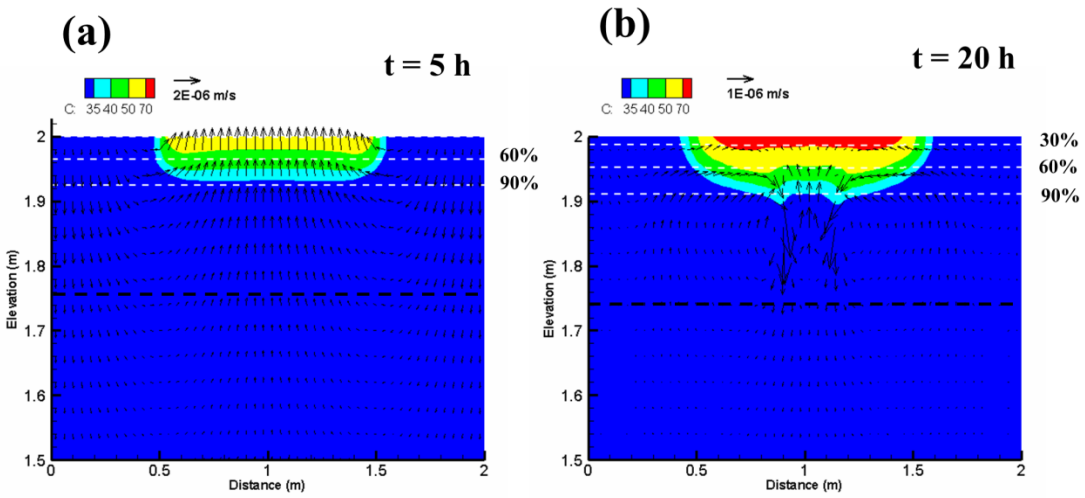

Figure 4.9 Simulated subsurface salinity contours, velocity field, and groundwater table for Scenario 1 at time t = 5 and 20 h. The white dashed lines represent soil moisture. The black dashed lines represent groundwater table. Vectors represent groundwater velocity.

Figures 4.10a and 4.10b show the simulated subsurface salinity contours, velocity field, and groundwater table for Scenario 2 at time t = 5 h and 20 h. As the water was evaporated from the soil surface, beneath the surface evaporation zone the groundwater table line dropped and the salinity increased, which induced a high salinity plume formed near the soil surface. As the presence of constant water table at the boundaries of the domain, the water table formed a concave curve during the evaporation process. Almost the same flow pattern and water table curve at two different times indicate that evaporation-induced hydraulic exchange between groundwater system and atmosphere

nearly reached a steady state. The concave shape of groundwater table generated a hydraulic gradient, which would drive groundwater flow to the evaporation zone. Then, the groundwater flowed upwards to the soil surface to provide the water for the evaporation process. The pattern of groundwater flow and associated subsurface solute distribution were different when comparing between Scenario 1 and 2. In Scenario 2, the constant water table provided a steady water supply for the evaporation at soil-air interface. Therefore, the groundwater flow pattern was always upward; however, in Scenario 1, in absence of water supply to the evaporation zone, after the water content at soil surface nearly reached equilibrium with atmospheric condition, evaporation-induced upward groundwater flow pattern disappeared and local groundwater circulation was formed due to salt precipitation. The comparison between the two scenarios indicates that salt accumulation would be more intensive and extensive when the surrounding area could provide groundwater recharge to the evaporation zone. After 20 hours, the averaged salinity within the area 0.2 m below the evaporation zone was ~44 g/L for Scenario 1 and ~52 g/L for Scenario 2. Also, at time t = 20 h, the plume expanded further downwards in Scenario 2. These behavior probably due to the fact that the presence of surrounding water supply caused a larger evaporation rate at soil surface and higher moisture distribution beneath the soil surface, which would extract more water from the soil and intensified the molecular diffusion of the plume.

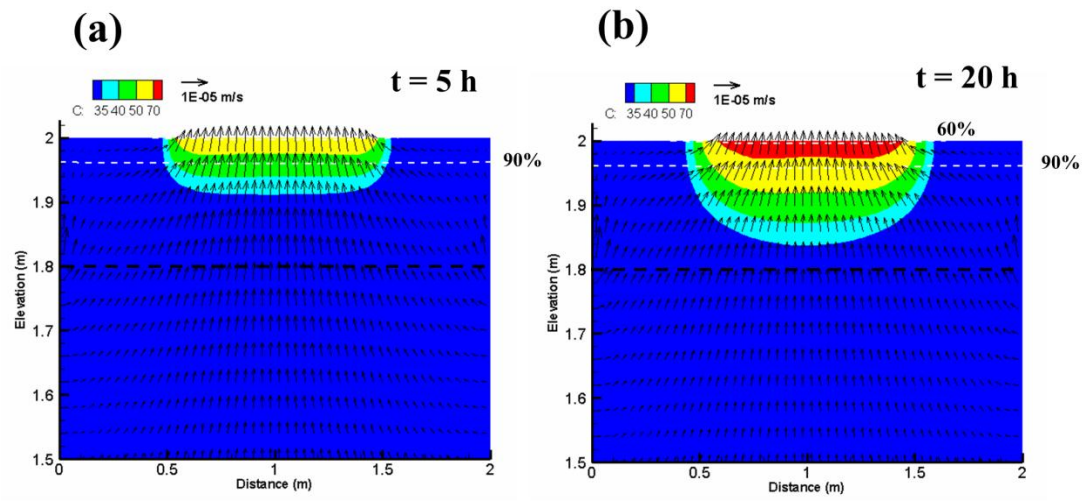

Figure 4.10 Simulated subsurface salinity contours, velocity field, and groundwater table for Scenario 2 at time t = 5 and 20 h. The white dashed lines represent soil moisture. The black dashed lines represent groundwater table. Vectors represent groundwater velocity.

4.5.2.4 Permeability Effect. The simulations were conducted to test the effect of different soil permeability on groundwater flow pattern and subsurface solute distribution for each scenario. Three values of soil permeability (5×10^{-4} m/s, 1×10^{-3} m/s, and 2×10^{-3} m/s) were considered herein. Figures 4.11a and 4.11b shows the salinity distribution profiles at time t = 20 h. The subsurface salinity distribution is different in both scenarios under the different soil permeability conditions. The results indicate that, when the soil permeability was higher, the upper salinity plume was less dense near the soil surface and expanded further downward. In Scenario 2, the salinity distribution was always lower for the higher soil permeability case. The plausible explanation is as follows: In Scenario 1, as the specific humidity tended to be equilibrium with atmospheric condition, the downward movement of salt was driven by density-dependent groundwater flow. Therefore, the salt would propagate downward faster in the higher permeability soil. In Scenario 2, as the domain is initially saturated by irrigation/submergence and the water table was set as a constant at the

boundaries (0.2 m below the surface), the initial drainage of the groundwater system would be the result of water discharge to the surrounding area and the evaporation from the soil surface. When the permeability is higher in the soil, more water would be discharged to the surrounding area. As the groundwater system drained the same amount of water, less amount of water would be evaporated from the soil surface, which led to lower salinity upper plume below the evaporation zone.

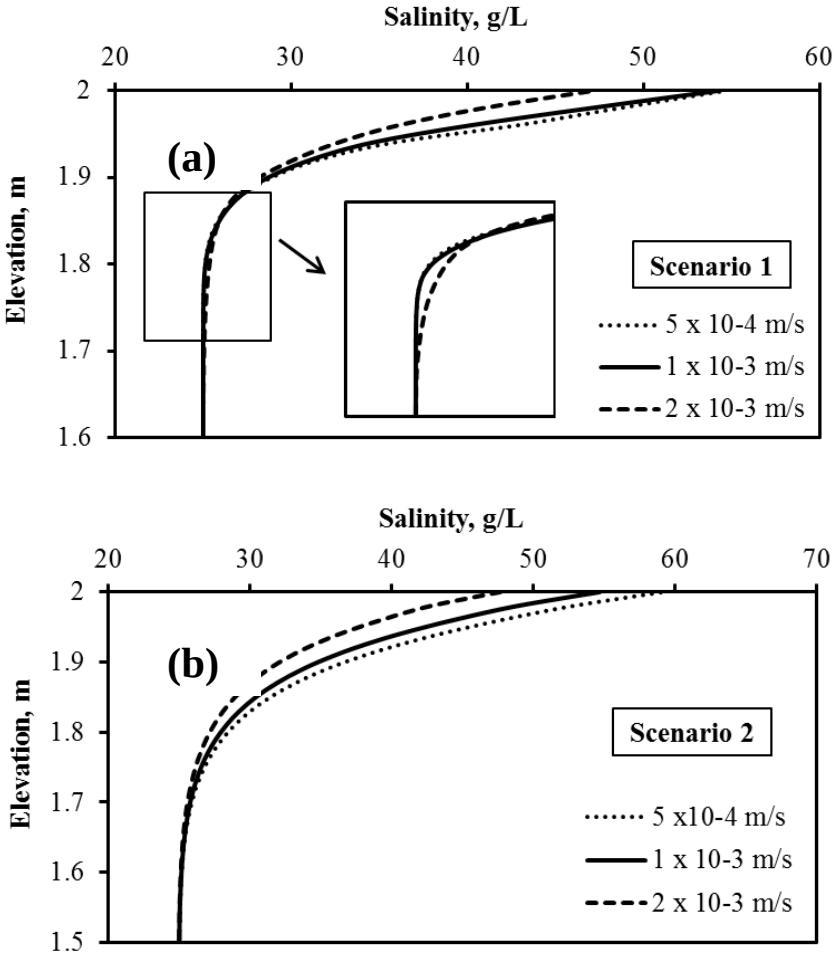

Figure 4.11 Simulated salinity distribution below the soil surface with different soil permeability for Scenario 1 (a) and Scenario 2 (b). The salinity is the horizontal average at each specific depth.

In contrast, under different soil permeability conditions, the moisture distribution has almost the same profile for both scenarios. The results are not shown in here for brevity. The plausible explanation could be found from Equation (2.3). The analytical expression (equation (2.3)) indicates that the soil moisture ratio is dependent of soil capillarity (van Genuchten parameter α, *n*, and S_r) and pressure head. The values of capillary parameters were fixed (α = 4.75, n = 8.5, and S_r = 0.07) for all the permeability tests; meanwhile, after the soil evaporation zone tended to reach the equilibrium with atmosphere, the variation of pressure head at each specific depth was related to water density change. Figure 4.12 shows that the variation of moisture ratio as a function of water density at three specific depths (soil surface, 0.05 m below the soil surface, and 0.1 m below the soil surface). As the water density increases from 25 g/L to 60 g/L (the maximum value for all the simulations at time t = 20h), the moisture ratio decreases 2%, 4%, and 10% at soil surface, 0.05 m below the surface, and 0.1 m below the surface, respectively. It could explain the results that the moisture ratio profile had almost the same distribution under different permeability conditions.

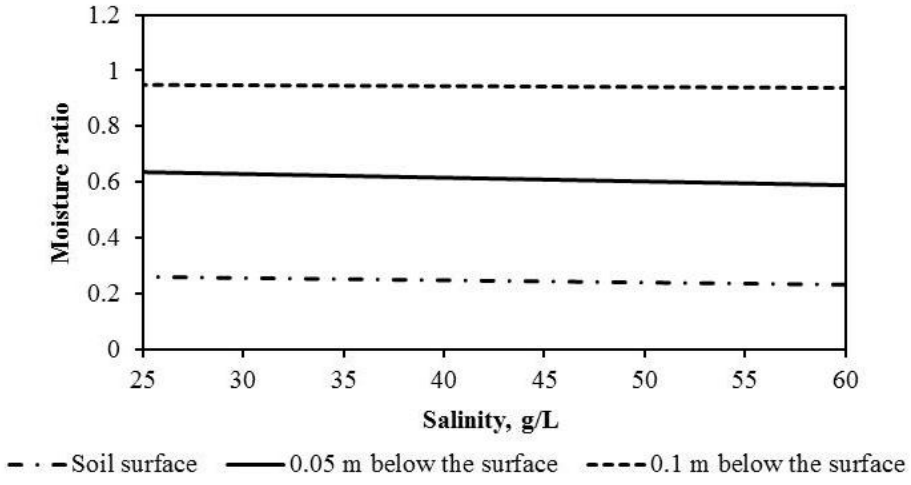

Figure 4.12 The variation of moisture ratio as a function of water density at three specific depths (soil surface, 0.05 m and 0.1 m below the soil surface).

4.5.2.5 Capillarity Effect. In order to reveal the effect of soil capillary on subsurface solute distribution, we considered the capillary drive (CD) (Morell-Seytoux et al., 1996), given by:

$$H_{cM} = (\frac{1}{\alpha})\frac{1}{(p-1)}(\frac{147.8+8.1p+0.092p^2}{55.6+7.4p+p^2}), \quad (4.11)$$

where H_{cM} is effective capillary drive, and the equivalent parameter, *p*, is expressed by

$$p = 1+2/m, \quad (4.12)$$

and we considered three situations corresponding to the following values of α (2.38 m^{-1}, 4.75 m^{-1}, and 9.5 m^{-1}), which give the value of capillarity drive equal to 42 cm, 21 cm, and 10 cm, respectively.

Figure 4.13a shows the soil moisture distribution profile at time t = 20 h for Scenario 1. Under different condition of soil capillary fringe, the subsurface moisture distribution is significantly different except for the soil moisture at the surface. As the specific humidity at the soil-air interface reached equilibrium, the water content at soil surface would be equal to that in atmosphere. The atmosphere condition was the same for the three situations (specific humidity = 0.2). Therefore, a large CD (α value is smaller), would result in a lower groundwater table. The same value of surface water content also indicates that without surrounding water supply to the evaporation zone, the soil surface water content was dependent of atmospheric condition. After the surface specific humidity at soil-air interface reached equilibrium, the subsurface moisture distribution profile and associated groundwater table were strongly related to soil capillary properties. It was

proven that the inverse of α has a proportional relationship with the length of soil capillary fringe. After the soil surface moisture reached equilibrium with atmospheric condition, the drawdown of groundwater table would be more intensive in the soil with higher capillary fringe. Therefore, the unsaturated zone would extend further downwards for the case of smaller α. Similarly, it is shown in Figure 4.13b that the soil moisture distribution profile was significant different under different capillarity soil conditions in Scenario 2. As the water table at the boundaries was constant in Scenario 2, the surface water content would be higher when the soil has a larger capillary fringe (smaller value of α), which is consistent with the simulation results. The different water content at soil surface would lead to a different humidity gradient at soil-air interface. The results also indicate that the soil capillarity properties would impact the evaporation rate at soil surface and associated subsurface upward groundwater flow when the evaporation zone has a sufficient surrounding water supply.

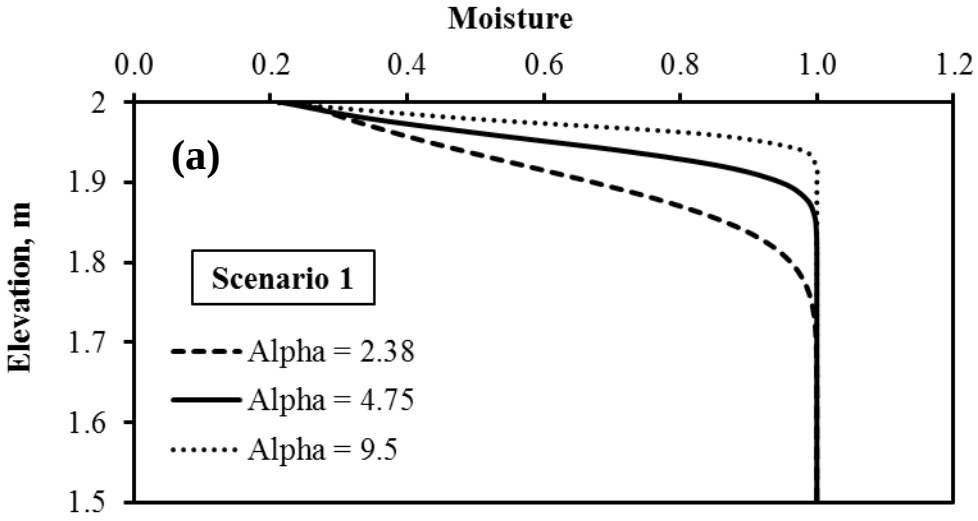

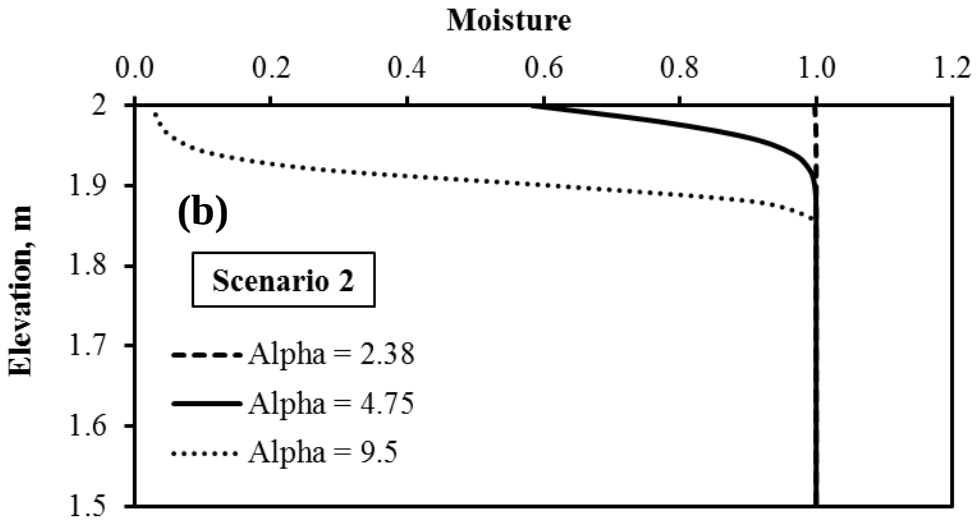

Figure 4.13 Simulated moisture distribution below the soil surface with different soil capillarity for Scenario 1 (a) and Scenario 2 (b). The soil moisture ratio is the horizontal average at each specific depth.

Figures 4.14a and 4.14b shows salinity distribution profile for each scenario under different soil capillarity conditions. The results indicate that in the soil with larger capillary fringe, salt accumulation beneath the evaporation zone is more intensive and the salt profile expanded further downwards for both scenarios. As shown in Figure 4.14a, in Scenario 1, the drawdown of water table was more extensive in the soil with larger capillary fringe. It indicates that evaporation would extract more water from the soil. Subsequently, more salt would be accumulated beneath the evaporation zone. Similarly, in Scenario 2, more water would be extracted from the soil surface due to a larger evaporation flux when a higher capillarity fringe existed in the soil. Therefore, a larger and denser salt plume would be formed beneath the evaporation zone in the soil with large capillary fringe.

The results show that in terms of management coastal aquifers, providing partial coverage of the soil might not be sufficient to minimize the amount of salt forming on the

soil surface. This is because the partial coverage creates zones that would play the equivalent of Scenario 2. The spacing of these areas would depend on soil properties.

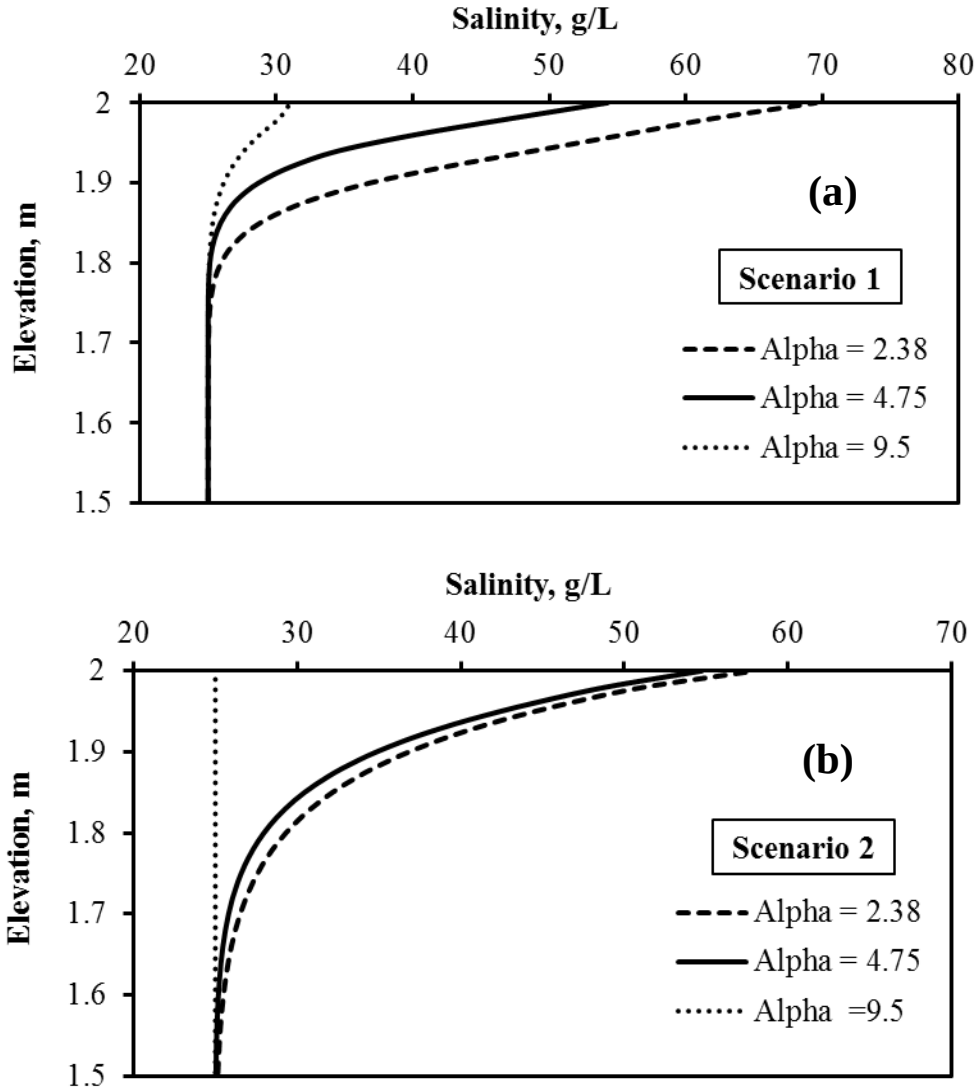

Figure 4.14 Simulated salinity distribution below the soil surface with different soil capillarity for Scenario 1 (a) and Scenario 2 (b). The salinity is the horizontal average at each specific depth.

4.6 Conclusion

It has been found that evaporation over bare soil plays an important role in groundwater flow and subsurface transport processes. A numerical study was conducted in this study to investigate groundwater flow and salt transport in bare saline soil subjected to transient evaporation. The simulation results showed that:

(1) Evaporation induced an upward groundwater flow pattern, which led to formation of an upper high saline plume beneath the evaporation zone. The plume expanded further downwards during the evaporation process.

(2) The presence of surrounding water supply significantly affected the velocity magnitude of the upward water flow and the density and extension of the plume. The presence of the surrounding water supply could provide a steady water flow to the evaporation zone and generated a steady evaporation rate at soil surface. As the dominated water flow pattern is in upward direction, the downward migration of plume is a result of molecular diffusion.

(3) In absence of the surrounding water supply, density-dependent flow would dominate groundwater dynamics after the specific humidity at the soil-air interface nearly reached equilibrium. The evaporation-induced density gradient generated pore water circulations around the plume edge and caused salt to migrate downwards with “finger” shapes.

(4) In absence of the surrounding water supply, the permeability of soil demonstrated a significant impact on solute fates when the soil specific humidity at surface reached equilibrium with atmospheric condition. In the case of higher permeability of soil, the evaporation-induced upper saline plume would expand further downward with less density. With surrounding water supply, higher permeability would allow water to discharge to surrounding area faster after the initial irrigation/submergence of the evaporation zone. It would cause less water evaporated from the soil surface and subsequently decrease the density and extension of the upper saline plume.

(5) The effects of soil capillarity on groundwater flow and solute transport were significant for both scenarios. Under the same atmospheric condition, larger capillary fringe would allow evaporation to extract more water from the soil. It would generate a larger and denser saline plume beneath the evaporation zone.

CHAPTER 5

CONCLUSIONS AND FUTURE WORK

The focus of this work was on the analyses of two important physical factors, oceanic waves and evaporation, on the groundwater flow and subsurface solute fate in coastal aquifers. The investigation was carried out through two separate studies: The first study consisted of simulating the behavior of groundwater flow and solute fate in coastal beaches subjected to waves. The simulation was validated against the observations in laboratory experiments conducted in Boufadel et al. (2007). As combined wave and tide forcing are more common oceanic forcing acting onto near-shore aquifer systems, a flow averaged approach was developed to quantify the combined forcing affecting coastal groundwater systems. The results suggested that wave forcing significantly impact the injected plume's trajectory, residence time, discharge zone and discharge rate. Separate wave forcing caused the plume to have a deeper trajectory in the beach and discharged at the groundwater table's exit point of the beach, while separate tide forcing caused the plume to migrate a longer pathway and discharged at the low tide zone of the beach. The combined wave and tide forcing seemed to have all the characteristics of separate oceanic forcing affecting subsurface solute fate in coastal aquifers. Under the combined forcing, due to waves, the plume migrated deeper, and the shape of plume was modified by seawater-groundwater circulations in the swash zone; due to tides, the trajectory length of the plume significantly increased and the plume discharged farther seaward at the low tide zone of the beach.

The second study performed a combined field and numerical study to quantify the effects of evaporation on groundwater flow and subsurface solute fates. The field

measurements demonstrated that evaporation generated a high salinity distribution at shallow layer of the beach. Numerical experiments suggested that evaporation induced an upward groundwater pattern, which led to formation of an upper high saline plume beneath the evaporation zone. As water was evaporated from the surface soil, the plume expanded further downwards. It is also found that the presence of surrounding water supply significantly affected the velocity magnitude of the upward water flow and the plume density and extension. Meanwhile, the surrounding water supply could provide a steady water flow to the evaporation zone and induce a steady evaporation rate at soil surface. As the dominated water flow pattern is in upward direction, the downward migration of plume is a result of molecular diffusion. In absence of surrounding water supply, it was expected that: (1) density-dependent flow would dominate groundwater dynamics after the specific humidity at the soil-air interface nearly reached equilibrium; (2) The evaporation-induced density gradient generated pore water circulations around the plume edge and caused salt to migrate downwards with "finger" shapes. It was found that soil permeability significantly impacted groundwater dynamics in the evaporation zone. In absence of the surrounding water supply, high permeability soil would allow evaporation-induced upper saline plume to expand further downward with less density. With surrounding water supply, high permeability would allow water to discharge to surrounding area faster after the initial irrigation/submergence of the evaporation zone. It would cause less water evaporated from the soil surface and subsequently decrease the density and diminished the extension of the upper saline plume. The effects of soil capillarity on groundwater flow and solute transport are significant for both scenarios. Under the same atmospheric condition,

evaporation would extract more water from the soil which has a larger capillary fringe. It subsequently generated a larger and denser salt plume beneath the evaporation zone.

Extending this work would obviously depend on the sought application. Nevertheless, from the vantage point we envisage the following steps:

1) Develop further improvements to deal with the effect of waves on beaches, including beaches with high hydraulic conductivity, which are cases that prevent running the hydrodynamic model and the subsurface flow model separately.

2) Account for the heterogeneity in coastal aquifers using a geostatistical framework. Existing approaches consider heterogeneity to occur at the large scale (i.e., layers). However, consider spatial variation in the hydraulic conductivity in some coastal aquifers could occur within centimeters.

3) Combine the MARUN model with a model that accounts for biotransformation. Such a combined model could apply to the degradation of dissolved organic carbon, and the uptake and subsequent release of nutrients by microorganisms in the pore water.

REFERENCES

Alley, W.M., Healy, R.W., LaBaugh, J.W. and Reilly, T.E., 2002. Flow and storage in groundwater systems. Science, 296(5575): 1985-1990.

Bakhtyar, R., Barry, D.A. and Brovelli, A., 2012a. Numerical experiments on interactions between wave motion and variable-density coastal aquifers. Coastal Engineering, 60: 95-108.

Bakhtyar, R., Brovelli, A., Barry, D.A., Robinson, C. and Li, L., 2012b. Transport of variable-density solute plumes in beach aquifers in response to oceanic forcing. Advances in Water Resources: 208-224.

Bakhtyar, R., Brovelli, A., Barry, D.A., Robinson, C. and Li, L., 2012c. Transport of variable-density solute plumes in beach aquifers in response to oceanic forcing. Advances in Water Resources.

Bakhtyar, R., Ghaheri, A., Yeganeh-Bakhtiary, A. and Barry, D.A., 2009. Process-based model for nearshore hydrodynamics, sediment transport and morphological evolution in the surf and swash zones. Applied Ocean Research, 31(1): 44-56.

Baldock, T. and Hughes, M., 2006. Field observations of instantaneous water slopes and horizontal pressure gradients in the swash-zone. Continental Shelf Research, 26(5): 574-588.

Barton, I., 1979. A parameterization of the evaporation from nonsaturated surfaces. Journal of Applied Meteorology, 18(1): 43-47.

Bobo, A.M., Khoury, N., Li, H. and Boufadel, M.C., 2012. Groundwater Flow in a Tidally Influenced Gravel Beach in Prince William Sound, Alaska. Journal of Hydrologic Engineering, 17(4): 494-494.

Boufadel, M.C., 2000. A mechanistic study of nonlinear solute transport in a groundwater-surface water system under steady-state and transient hydraulic conditions. Water Resources Research, 36: 2549-2566.

Boufadel, M.C., Li, H., Suidan, M.T. and Venosa, A.D., 2007. Tracer studies in a laboratory beach subjected to waves. Journal of Environmental Engineering, ASCE, 133(7): 722-732.

Boufadel, M.C., Suidan, M.T. and D, V.A., 1999a. A numerical model for density-and-viscosity-dependent flows in two- dimensional variably-saturated porous media. Journal of Contaminant Hydrology, 37: 1-20.

Boufadel, M.C., Suidan, M.T., Rauch, C.H., Venosa, A.D. and Biswas, P., 1998a. 2-D variably-saturated flow: Physical scaling and Bayesian estimation. Journal of Hydrologic Engineering, 3(10): 223-231.

Boufadel, M.C., Suidan, M.T. and Venosa, A.D., 1998b. 2-D variably-saturated flow: Physical scaling and Bayesian estimation. Journal of Hydrologic Engineering, ASCE, 3: 223-231.

Boufadel, M.C., Suidan, M.T. and Venosa, A.D., 1999b. Numerical modeling of water flow below dry salt lakes: effect of capillarity and viscosity. Journal of Hydrology, 221: 55-74.

Boufadel, M.C., Xia, Y. and Li, H., 2011. Modeling solute transport and transient seepage in a laboratory beach under tidal influence. Environmental Modelling & Software, 26(7): 899-912.

Bradshaw, M., 1974. High frequency water table fluctuations and mass movement on sandy beaches. BA Honours Thesis, Department of Geography, Australian National University, 122pp.

Calow, R., Robins, N. S., Macdonald, A. M., Macdonald, D. M. J., Gibbs, B. R., Orpen, W. R. G., Mtembezeka, P., Andrews, A. J., Appiah, S. O., 1997. Groundwater management in drought-prone areas of Africa. International Journal of Water Resources Development, 13(2): 241-262.

Chattopadhyay, N. and Hulme, M., 1997. Evaporation and potential evapotranspiration in India under conditions of recent and future climate change. Agricultural and Forest Meteorology, 87(1): 55-73.

Elder, J.W., 1967. Transient convection in a porous medium. Journal of Fluid Mechanics, 27(3): 609-623.

Frolkovič, P. and De Schepper, H., 2000. Numerical modelling of convection dominated transport coupled with density driven flow in porous media. Advances in Water Resources, 24(1): 63-72.

Geng, X., Boufadel, M.C. and Wrenn, B., 2013. Mathematical modeling of the biodegradation of residual hydrocarbon in a variably-saturated sand column. Biodegradation, 24(2): 153-163.

Goseberg, N., Wurpts, A. and Schlurmann, T., 2013. Laboratory-scale generation of tsunami and long waves. Coastal Engineering, 79: 57-74.

Guo, Q., Li, H., Boufadel, M.C. and Sharifi, Y., 2010. Hydrodynamics in a gravel beach and its impact on the Exxon Valdez oil. Journal of Geophysical Research, 115.

Hancock, P.J., Boulton, A.J. and Humphreys, W.F., 2005. Aquifers and hyporheic zones: towards an ecological understanding of groundwater. Hydrogeology Journal, 13(1): 98-111.

Hirt, C.W. and Nichols, B.D., 1981. Volume of fluid (VOF) method for the dynamics of free boundaries. Journal of Computational Physics, 39(1): 201-225.

Horn, D., Baldock, T., Baird, A. and Mason, T., 1998. Field measurements of swash induced pressures within a sandy beach. Coastal Engineering Proceedings, 1(26).

Horn, D.P., 2006. Measurements and modelling of beach groundwater flow in the swash-zone: a review. Continental Shelf Research, 26(5): 622-652.

Il'Ichev, A.T., Tsypkin, G.G., Pritchard, D. and Richardson, C.N., 2008. Instability of the salinity profile during the evaporation of saline groundwater. Journal of Fluid Mechanics, 614: 87-104.

Kang, H.-Y., Nielsen, P. and Hanslow, D.J., 1994. Watertable overheight due to wave runup on a sandy beach. Coastal Engineering Proceedings, 1(24).

Kersten, M., Leipe, T. and Tauber, F., 2005. Storm disturbance of sediment contaminants at a Hot-Spot in the Baltic Sea assessed by 234Th radionuclide tracer profiles. Environmental Science & Technology, 39(4): 984-990.

Lee, T.J. and Pielke, R.A., 1992. Estimating the soil surface specific humidity. Journal of Applied Meteorology, 31: 480-480.

Li, Barry, D.A., Parlange, J.Y. and Pattiaratchi, C.B., 1997. Beach water table fluctuations due to wave run-up: capillarity effects. Water Resources Research, 33(5): 935-945.

Li, H., Boufadel, M.C. and Weaver, J.W., 2008. Tide induced seawater-groundwater circulation in shallow beach aquifer. Journal of Hydrology, 352: 211-224.

Li, L. and Barry, D., 2000. Wave-induced beach groundwater flow. Advances in Water Resources, 23(4): 325-337.

Li, L., Barry, D., Pattiaratchi, C. and Masselink, G., 2002. BeachWin: modelling groundwater effects on swash sediment transport and beach profile changes. Environmental Modelling & Software, 17(3): 313-320.

Liu, G., Yang, J. S., He, L. D., Lv, Z. Z., Shao, H. B., and Yu, S. P., 2013. Salt dynamics in soil profiles during long-term evaporation under different groundwater conditions. Plant Biosystems-An International Journal Dealing with all Aspects of Plant Biology, 147(4): 1211-1218.

Liu, S., Mao, D. and Lu, L., 2006. Measurement and estimation of the aerodynamic resistance. Hydrology and Earth System Sciences Discussions, 3(3): 681-705.

Longuet-Higgins, M.S., 1983. Wave set-up, percolation and undertow in the surf zone. Proceedings of the Royal Society of London. A. Mathematical and Physical Sciences, 390(1799): 283-291.

Mahfouf, J. and Noilhan, J., 1991. Comparative study of various formulations of evaporations from bare soil using in situ data. Journal of Applied Meteorology, 30(9): 1354-1365.

Mahrt, L., 1996. The bulk aerodynamic formulation over heterogeneous surfaces, Boundary-Layer Meteorology 25th Anniversary Volume, 1970–1995. Springer, pp. 87-119.

Mahrt, L. and Ek, M., 1984. The influence of atmospheric stability on potential evaporation. Journal of Climate Applied Meteorology and Climatology.

Menziani, M., Pugnaghi, S., Pilan, L., Santangelo, R. and Vincenzi, S., 1999. Field experiments to study evaporation from a saturated bare soil. Physics and Chemistry of the Earth, Part B: Hydrology, Oceans and Atmosphere, 24(7): 813-818.

Michael, H.A., Mulligan, A.E. and Harvey, C.F., 2005. Seasonal oscillations in water exchange between aquifers and the coastal ocean. Nature, 436(7054): 1145-1148.

Moore, W.S., 1996. Large groundwater inputs to coastal waters revealed by 226Ra enrichments. Nature, 380: 612–614.

Morell-Seytoux, H.J. et al., 1996. Parameter equivalence for the Brooks-Corey and van Genuchten soil characteristics: Preserving the effective capillary drive. Water Resources Research, 32(, no. 5): 1251-1258.

Narayan, K.A., Schleeberger, C. and Bristow, K.L., 2007. Modelling seawater intrusion in the Burdekin Delta irrigation area, North Queensland, Australia. Agricultural Water Management, 89(3): 217-228.

Nassar, I. and Horton, R., 1989. Water transport in unsaturated nonisothermal salty soil: I. Experimental results. Soil Science Society of America Journal, 53(5): 1323-1329.

Nielsen, P., 1999. Groundwater dynamics and salinity in coastal barriers. Journal of Coastal Research: 732-740.

Oldenburg, C.M. and Pruess, K., 1995. Dispersive transport dynamics in a strongly coupled groundwater-brine flow system. Water Resources Research, 31(2): 289-302.

Robinson, C., Brovelli, A., Barry, D. and Li, L., 2009. Tidal influence on BTEX biodegradation in sandy coastal aquifers. Advances in Water Resources, 32(1): 16-28.

Robinson, C., Gibbes, B., Carey, H. and Li, L., 2007. Salt-freshwater dynamics in a subterranean estuary over a spring-neap tidal cycle. Journal of Geophysical Research, 112(C9): C09007.

Robinson, C., Gibbes, B. and Li, L., 2006. Driving mechanisms for groundwater flow and salt transport in a subterranean estuary. Geophysical Research Letters, 33: L03402, doi:10.1029/2005GL025247.

Rouxel, O., Sholkovitz, E., Charette, M. and Edwards, K.J., 2008. Iron isotope fractionation in subterranean estuaries. Geochimica et Cosmochimica Acta, 72(14): 3413-3430.

Santas, R. and Santas, P., 2000. Effects of wave action on the bioremediation of crude oil saturated hydrocarbons. Marine Pollution Bulletin, 40(5): 434-439.

Singh, V.P., 2002. Mathematical models of large watershed hydrology. Water Resources Publication.

Sous, D., Lambert, A., Vincent, R. and Michallet, H., 2013. Swash-groundwater dynamics in a sandy beach laboratory experiment. Coastal Engineering, 80: 122-136.

Tetens, O., 1930. Uber einige meteorologische Begriffe. Z. Geophys., 6: 297-309.

Turner, I.L. and Masselink, G., 1998. Swash infiltration-exfiltration and sediment transport. Journal of Geophysical Research: Oceans (1978–2012), 103(C13): 30813-30824.

Unver, O. and Mays, L.W., 1984. Optimal determination of loss rate functions and unit hydrographs. Water Resources Research, 20(2): 203-214.

van Genuchten, M.T., 1980. A closed-form equation for predicting the hydraulic conductivity of unsaturated soils. Soil Science Society of America Journal, 44(5): 892-898.

Vandegriend, A.A. and Owe, M., 1994. Bare Soil Surface-Resistance to Evaporation by Vapor Diffusion Under Semiarid Conditions. Water Resources Research, 30(2): 181-188.

Wetzel, P.J. and Chang, J.-T., 1987. Concerning the relationship between evapotranspiration and soil moisture. Journal of Climate and Applied Meteorology, 26(1): 18-27.

Wooding, R., Tyler, S.W. and White, I., 1997. Convection in groundwater below an evaporating salt lake: 1. Onset of instability. Water Resources Research, 33(6): 1199-1217.

Xin, P., Robinson, C., Li, L., Barry, D.A. and Bakhtyar, R., 2010. Effects of wave forcing on a subterranean estuary. Water Resources Research, 46(12).

Yakirevich, A., Berliner, P. and Sorek, S., 1997. A model for numerical simulating of evaporation from bare saline soil. Water Resources Research, 33(5): 1021-1033.

Zarei, G., Homaee, M. and Liaghat, A., 2009. Modeling transient evaporation from descending shallow groundwater table based on Brooks–Corey retention function. Water Resources Management, 23(14): 2867-2876.

Zghibi, A., Zouhri, L., Tarhouni, J. and Kouzana, L., 2012. Groundwater mineralisation processes in Mediterranean semi-arid systems (Cap-Bon, North east of Tunisia): hydrogeological and geochemical approaches. Hydrological Processes.